SOL-GEL SYNTHESIS OF CALCIUM PHOSPHATE POWDERS

By

AHMED AHMED SARHAN

A Dissertation submitted to the

School of Graduate Studies

Rutgers, The State University of New Jersey

In partial fulfillment of the requirements

For the degree of

Doctor of Philosophy

Graduate Program in Materials Science and Engineering

Written under the direction of

Prof. Lisa C. Klein

And approved by

_____

_____

_____

_____

_____

New Brunswick, New Jersey

JANUARY 2019

ABSTRACT OF THE DISSERTATION

Sol-Gel Synthesis of Calcium Phosphate Powders

By AHMED AHMED SARHAN

Dissertation Director:

Lisa C. Klein

Materials that are used for biomedical or clinical applications are known as biomaterials. These materials are made in different forms according to their functionality and the body part they will repair. Biocompatibility, biofunctionality, and bioavailability are three significant factors in selecting these materials, as they might be bioinert, resorbable, or bioactive like hydroxyapatite.

Hydroxyapatite (HAp), chemical formula $Ca_{10}(PO_4)_6(OH)_2$, having a calcium to phosphorus ratio of 1.667, has received special interest in the field of biomaterials as it is well known to be an inorganic bioactive material capable of forming chemical bonds with bones and teeth, besides promoting tissue engineering and bone growth for the treatment of infected or damaged organs. It is chemically and crystallographically similar to the main minerals in bones, dentin, and enamel where no toxicity or inflammation of a foreign body response has occurred. Affinities of biopolymers, and the high osteogenic

potential of promoting bone in-growth and osteoconduction, are common reasons for synthetic HAp to dominate the field of biomaterials.

HAp ceramics are mostly limited to applications of low mechanical loads. In use, this may mean that the HAp is used in conjunction with a polymer in a composite. Consideration is given to using HAp powders in 3D printing. By using 3D printing, it is possible to control the pore size and pore distribution of composite scaffolds. Since the characteristics of the HAp powders influence the ability to print bone scaffolds, it is interesting to compare their properties.

There are numerous synthesis methods and approaches to produce HAp. In this study, hydroxyapatite is prepared by the sol-gel method, where precursors are subjected to high temperatures treatment after a gel-like network is formed. These powders are compared to HAp prepared by the hydrothermal method, where the precursors react in an aqueous solution under high temperature and pressure to synthesize HAp crystals. Both materials have been studied in comparison to a commercial HAp powder obtained from a manufacturer (FLUIDINOVA, S.A). This study focuses on the differences of preparation methodology, the resulting microstructures, phase composition, particle size and crystallinity.

The sol-gel method provided a homogeneous molecular mixing at a low processing temperature (<95°C). The resulting apatite structure mainly depended on the choice of the precursors and the sintering temperature. For comparison, the hydrothermal technique produced crystalline HAp in one step without requiring post heat treatment to crystallize. HAp formed directly from the aqueous solution in a sealed vessel at high pressure and temperature of 150°C.

Phase identification by X-ray diffraction analysis, microstructure analysis (FESEM), nitrogen surface area (BET), particle size, differential thermal analysis was performed on the samples of the HAp powders. Higher crystallinity, higher surface area, high pore volume, a narrow range of particle sizes, and a needle-like morphology point to the fact that hydrothermal HAp powder is a preferred choice for 3D printing applications.

Acknowledgments

At every beginning, all praise and gratitude to Allah for his mercy and divine guidance throughout every decision and milestone in my life, giving me the willingness, patience, and strength to succeed.

To my advisor Prof. Lisa C. Klein, thank you for the support and mentorship helping me write this dissertation and finish my Ph.D. degree. As well, many thanks to the thesis committee: Prof. Ahmad Safari, Prof. Adrian Mann, Prof. Andrei Jitianu, and Prof. Ashutosh Goel for their valuable inputs, insightful comments. Their recommendations indeed gave the work extra value.

My sincere thanks for Prof. Goel's research group for their collegial guidance, and for the opportunity to facilitate their research equipment. Their willingness, and ease, helped a lot in getting out the results of this research.

My extended appreciation to the Higher Committee of Education Development in Iraq (HCED) for this fellowship that brought me the opportunity to achieve a Ph.D. in the United States. Sincere appreciation to Uncle Kais Ebrahem, my guardian throughout this adventure in the States. Thanks to all my friends, relatives, colleagues, and the people of my home city "Hit" for their encouragement and honest wishes of success.

Never the least, my words of appreciation fall short in front of my parents and family. My Father's hand on my shoulder the moment I left to the airport is never forgotten. Their words in one voice, "we got your back, don't worry about anything, just make us proud" is still in my mind. Yes, this degree is to honor them for their love, prayers, inspiration, sacrifice, and commitment. My family set the ultimate example that I followed to complete this work. I am everlasting proud and thankful to be their son.

For the all of you, many thanks

Ahmed A. Sarhan, New Brunswick, NJ, 12th of October 2018

Dedicated to

To you, who taught me to compete with myself first,

my sanctuary, my role model, my father.

To the soul of my mother (RIP) who dreamed of this day,

the one who taught me that so much could be done with so little.

To my two brothers and their children,

I honor them with this humble effort.

Table of Contents

Chapter Three - Materials and Methods

Chapter Four - Results and Discussions

LIST OF FIGURES

LIST OF TABLES

LIST OF ABBREVIATIONS

HAp Hydroxyapatite

β-TCP Beta Tricalcium Phosphate

BCP Biphasic Calcium Phosphate Ceramics

PHEMA Poly (2-Hydroxyethyl Methacrylate)

PAA Polyacrylic Acid

PEI Polyethylenimine

CPC Calcium Phosphate Cement

PCL Poly Caprolactone

PEG Polyethylene Glycol

PlGA Poly Lactic-Co-Glycolic Acid

PVA Polyvinyl Alcohol

THF Tetrahydrofuran

DMF *N*,*N*-Dimethylformamide

Bis-GMA Bisphenol A Glycidyl Methacrylate

SBF Simulated Body Fluid

hMSC Marrow-Derived Mesenchymal Stem Cells

CTAB Cetyltrimethylammonium Bromide

XRD X-Ray Diffraction

FESEM Field Emission Scanning Electron Microscopy

TEM-EDX Dispersive X-Ray Spectroscopy

TG Thermogravimetric Analysis

DTA Differential Thermal Analysis

DSC Differential Scanning Calorimetry

FTIR Fourier Transform Infrared Spectroscopy

SD Standard Deviations

ADP Ammonium Dihydrogen Phosphate

SLS Selective Laser Sinering

SPS Spark Plasma Sintering

HIP Hot Isostatic Pressing

Chapter One

Introduction

1.1 Introduction

Materials that are used for biomedical or clinical applications are known as biomaterials. These materials are made in different forms according to what functionality and body part they will repair. Biocompatibility, biofunctionality, and availability are three significant factors in selecting these materials, as they might be bioinert (e.g., alumina and zirconia), resorbable (e.g., tricalcium phosphate), bioactive (e.g., hydroxyapatite, bioactive glasses, and glass-ceramics), or porous for tissue ingrowth (e.g., hydroxyapatite-coated metals) [1].

Hydroxyapatite (HAp), chemical formula $Ca_{10}(PO_4)_6(OH)_2$, has received special interest in the field of biomedical engineering. In addition to Bioactive Glass, HAp is well known to be a bioactive material capable of forming chemical bonds with bones and teeth. It is chemically and crystallographically similar to the main minerals in bones, dentin, and enamel [2]. Besides being the coating of choice for surgical metal and an alternative to polymer coatings, HAp is promoted for tissue engineering in the treatment of sick or lost organs. In this case, scaffolds are designed to serve as a temporary adhesive substrate for embedded cells promoting their growth, and a physical support for the arrangement of the new organ. These scaffolds need to be biocompatible, biodegradable, porous with a high surface/volume ratio, and mechanically sound [3].

Apatite is a general term for the crystalline minerals that have the formula $M_{10}(ZO_4)_6X_2$. Different ions shown in table 1 might replace the (M, ZO_4 and X) components and still be called apatite.

However, the most common apatite found in nature is calcium phosphate apatite, where M and ZO_4 are Ca^{2+} and PO_3^{-4}, respectively. When X is –OH, i.e. $Ca_{10}(PO_4)_6(OH)_2$, stoichiometric Ca/P molar ratio 1.67, the apatite is called Hydroxyapatite (HAp) [4].

Table 1. Major ions that can be part of apatite, $M_{10}(ZO_4)_6X_2$

Component	**Ions**
M	Ca^{2+}, Mg^{2+}, Sr^{2+}, Ba^{2+}, Mn^{2+}, Fe^{2+}, Zn^{2+}, Cd^{2+}, Pb^{2+}, H^{+}, Na^{+}, K^{+}, Al^{3+}, etc.
ZO_4	PO_4^{3-} , AsO_4^{3-}, VO_4^{3-}, SO_4^{3-}, CO_3^{2-}, SiO_4^{3-}, etc.
X	OH^{-}, F^{-}, Cl^{-}, Br^{-}, O^{2-}, CO_3^{2-} , etc.

Hydroxyapatite can be synthesized via several methods such as wet chemical deposition, biomimetic deposition, sol-gel route (wet-chemical precipitation) or electro deposition [5]. Yagai and Aoki proposed a wet chemical precipitation reaction that formed a hydroxyapatite nanocrystal suspension [6].

$$10\ Ca(OH)_2 + 6\ H_3PO_4 \rightarrow Ca_{10}(PO_4)_6(OH)_2 + 18\ H_2O \ldots\ldots \qquad \text{eq (1)}$$

Since calcium phosphate (CaP) salts are the principal mineral constituents of bones, hydroxyapatite ($Ca_{10}(PO_4)_6(OH)_2$, is the most thermodynamically stable crystalline phase of CaP in body fluid. For decades, synthetic HAp has been widely used mostly due to its excellent biocompatibility and bioactivity, where no toxicity or inflammation of a foreign body response has occurred. Affinities of biopolymers, and the high osteogenic potential of promoting bone ingrowth and osteoconduction, are

common reasons for synthetic HAp to dominate the field of biomaterials [7] in the use of bone replacement, augmentation, and for coating metal prostheses to improve their biocompatibility [8]. The mineral of bones and teeth is an impure form of HAp, having a variable Ca/P mol ratio of (1.6 to 1.7), as well a low percentage of CO_3^{2-} and water. The microcrystals in HAp are approximately 150Å wide by 400Å long in bone and dentin, and 400Å wide or more in dental enamel [8].

The structure of the apatite, $Ca_{10}(PO_4)_6F_2$, is an approximate hexagonal close packed set of spheres in which each sphere represents a tetrahedral PO_4^{3-} ion. This packing has octahedral interstitial sites that form channels through the structure parallel to the hexagonal axis. The F^- and 4/10ths of the Ca^{2+} ions are in these channels forming columns of F^- and Ca^{2+} ions. The remaining 6/10ths of the Ca^{2+} ions form Ca triangles around the F^- ions [9].

Fig 1.1 Structure of Hydroxyapatite

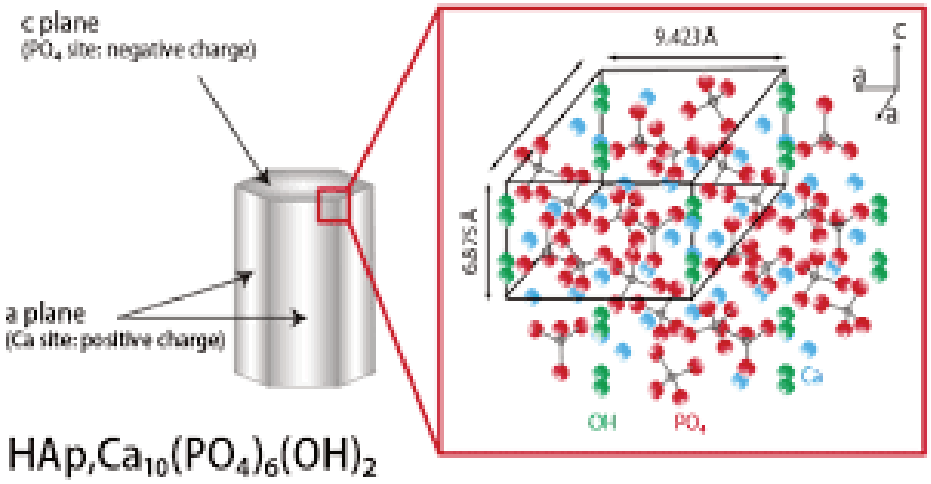

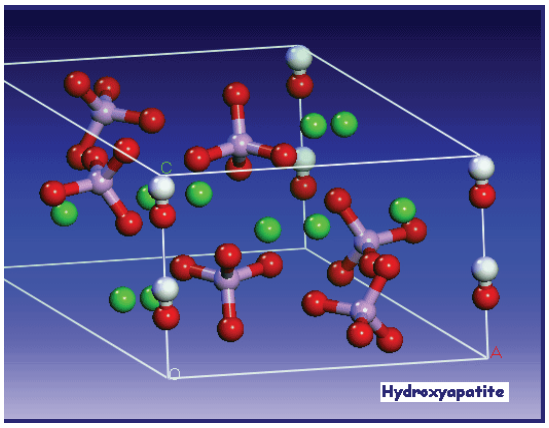

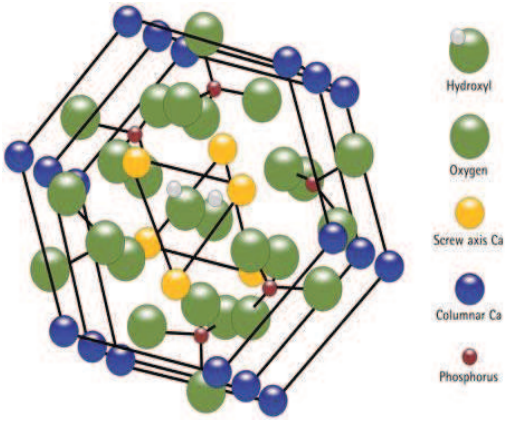

To date, calcium phosphate HAp is produced for clinical purposes in different forms and several composites with a poorly crystallized non-stoichiometric apatite phase containing CO_3^{2-}, Na^+, F^- and other ions in collagen fiber matrix calcium in the presence of bone. Research on new HAp formulations is being carried out to approach the nanosized and monolithic structures that make the material more effective for biomedical applications [9]. In the biologically active process whereby the HAp layer binds with normal bone, HAp needs to be partially soluble. Coatings that are less crystalline and more soluble are better when it comes to fusing with bone [9]. Due to the chemical similarity of calcium phosphates in HAp to bones, it is integrated into 3D printed structures used for tissue engineering and bone replacements [10].

Currently, HAp is the material of choice for various biomedical applications, e.g. replacement for bone and periodontal defects, alveolar ridge, middle ear implants, tissue engineering systems, drug delivery agents, dental materials, and bioactive coatings [7]. Nanosized HAp is used because of better resorbability, higher bioactivity, less demineralization, improved densification and sinterability due to higher surface energy [11].

Nonmedical, industrial, and technological uses of HAp include catalysts for chemical reactions such as the Michael-type addition and methane oxidation, host materials for lasers, fluorescence

materials, ion conductors, and gas sensors. Synthetic HAp is used in column chromatography for simple and rapid fractionation (isolating) of proteins and nucleic acids, water treatment, and remediation of heavy metal contaminated soils, grinding media, and light-weight concrete [6,7]. Moreover, HAp has been used to adjust and stabilize the corrosion rate of magnesium alloys in the form of metal matrix composites resulting in a cyto-compatible, biodegradable material [12]. HAp is used in absorbing and decomposing CO in composite air filters, and as an adsorbent for fluoride. The biocomposite removes fluoride through an ion-exchange mechanism and is both biocompatible and biodegradable [13].

There are numerous synthesis methods to produce HAp [14]. In this thesis, two methods were used and compared. First, the Sol-Gel method was used, where precursors are subjected to high temperatures after a gel-like network is formed to attain spherical shape HAp nanoparticles [15]. Second, the Hydrothermal method was used, where the precursors are reacted in an aqueous solution under high temperature and pressure to synthesize HAp crystals [16,17].

Other HAp synthesis approaches use conventional synthesis techniques such as: chemical approach; wet chemical precipitation method, where the reaction of precursors produces a precipitate of HAp nano-plate like morphology [18,19]; and solid-state reaction method, where the precursors are sintered at high temperatures to obtain micro and nano-particles [20,21]. There are mechanical approaches such as mechanochemical methods, which involve coupling of mechanical forces and chemical reactions to obtain nanorods and/or nanofibers [22,23]. In the biomimetic deposition approach, the precursors are added to synthetically prepared simulated body fluid (SBF) and ultrasonically irradiated to obtain micro-sized HAp particles [24,25]. Electrodeposition methods use electric current to form nano-sized HAp coatings on an electrode [26,27]. In the complexing approach, polymers such as polyethylene glycol are added along with the precursor solutions and a reaction is carried out similar to wet chemical precipitation to obtain HAp nanoparticles [28,29]. Other

miscellaneous methods include emulsion methods, where aqueous solvents containing the precursors are mixed with organic solvents containing surfactants to obtain HAp nanospheres [30,31], and ultrasonic spray pyrolysis methods, where precursor solution is directed through an ultrasonic nozzle on a substrate to produce HAp nano-rods [32,33].

The physical and chemical properties of HAp differ from one synthesis technique to another, with respect to different applications. Therefore, powder or coating characteristics of the procedure should be decided before choosing the technique. The ease of scalability and cost are main factors to consider for large scale quantities.

Chapter Two

Literature Review

There are many studies related to different techniques of synthesizing calcium hydroxyapatite. Several methods have been used for the synthesis of HAp including dry methods (solid state and mechano-chemical techniques), wet chemical methods (precipitation, hydrolysis, sol-gel approach, hydrothermal synthesis, multiple emulsion, biomimetic deposition, and electrodeposition), and high temperature process (combustion, pyrolysis, biogenic sources) [7,34].

1. Synthesis Methods

a. Precipitation

Precipitation is the most widespread approach due to its simplicity, low reaction temperature, minimal operating costs, ready availability and use of inexpensive raw materials [35]. This process is attractive to manufacturing applications due to its scalability. Obtaining a final homogeneous product takes controlling the solution pH, concentration, and temperature of the mixture when it reaches supersaturation. The post-formation precipitated powders are typically calcined at 400-600°C to refine the crystal structure, and in some cases fully crystallized HAp is not formed until it has been sintered up to 1200°C. A main consideration is that, simultaneous nucleation, crystal growth, coarsening and/or agglomeration occur once the solution is supersaturated [35]. Therefore, this technique requires fine-tuning to optimize morphology and minimize

crystal growth. Several surfactants (e.g. PVA) or dispersants (e.g. ammonium polyacrylate, ethanolamine) have been used to reduce particle agglomeration [35, 36].

b. Sol-Gel Approach

The sol-gel method is a technique of homogeneous molecular mixing and low processing temperatures (<400°C) with the ability of synthesizing nano-sized particles. This method includes two stages: forming the 'sol', which is a dispersion of solid particles, also known as colloids in a liquid, and the 'gel', which can be defined as a diphasic system consisting of a solid and interstitial liquid phase. Gelation is the process of linking monomer unites together through the condensation of OH^- forming M-O-M bonds within the sol causing the viscosity to increase. Gelation occurs by hydrolysis and polycondensation reactions.

Precursor materials are mechanically mixed in a solvent at a pH that prevents precipitation. Typical precursors are metal alkoxides (e.g. tetraethoxysilane to introduce silicon) and metal salts (e.g. calcium nitrate to add calcium, and ammonium phosphate to add phosphorus) [35]. Some reactants are costly as compared to other low temperature methods [37].

Post gelation, a drying process is necessary to remove the liquid phase. Drying is usually accompanied by a significant amount of shrinkage. During drying, the gel can break into small pieces, which results in a fine powder for further processing as a granulate. In comparison, aging the gel before drying and specific sintering protocols are essential to avoid cracking in 3D structures [35].

The sol-gel method is an effective method for the synthesis of nanophasic HAp, due to the possibility of controlling the process parameters and having a molecular level mixing of the calcium and phosphorus. It has been reported that HAp materials synthesized by sol-gel process are effective in improving the contact and stability at the artificial/natural bone interfaces in both in vitro and in vivo environment [34]. Several calcium and phosphorus precursor combinations were used for sol-gel synthesis of HAp. The resulting apatite structure mainly depends on the chemical nature of those precursors in terms of chemical activity and required formation temperatures. Balamurugan et al. [38] used $Ca(NO_3)_2.4H_2O$ and triethyl phosphate as calcium and phosphorus precursors, to obtain the stoichiometric Ca/P ratio 1.67. The synthesized HAp powders were dried and calcinated at temperatures up to 900°C. Brendel et al. [5] synthesized HAp using $Ca(NO_3)_2.4H_2O$ and phenyl dichlorophosphite [$C_6H_5PCl_2$] as precursors at (400°C) resulting in a low purity and poor crystallinity powder. However, increasing the temperature up to 900°C formed a pure, well-crystallized HAp phase. In another approach, Vijayalakshmi et al. [39] synthesized microcrystalline HAp powders from calcium acetate and triethyl phosphate in water and ethanol medium. They showed that proper heat and acid treatment could eliminate secondary phases such as CaO, $Ca_2P_2O_7$, and tricalcium phosphate (β-TCP) by managing the pH and gelation time. The acid treated powder showed better resolved HAp peaks at 211, 112, and 300 planes. The acid consumes all the soluble impurities, and the calcium carbonate peak at 29.399° was minimized by a mild acid washing method.

Flores et al. [40] studied the influence of mixing techniques on sol-gel synthesized HAp powders using calcium precursor $Ca(NO_3)_2 .4H_2O$ at room temperature.

Powder characterization showed that samples synthesized under ultrasonic mixing at a higher addition rate (12 drop/min) had more compact surface morphology and no tendency to absorb atmospheric carbon, as compared to the sample synthesized by continuous stirring and lower addition rate (6 drop/min). Thermal diffusivity values for the ultrasonically mixed samples gave a value closer to the typical value for thermal effusivity of mandibular human bone. As the higher mixing rate and ultrasonic technique produce an appropriate stoichiometry, and a homogeneous granular surface, as seen in an SEM study of the surface morphology, these powders are more suitable for biomedical applications such as bioactive coatings or bone cements. Flores stated that a higher addition rate and ultrasonic agitation prevented the increase of crystallite size by adding energy to the system during the chemical reaction, which makes the chemical reaction faster at a fixed pH value. In comparison, the slower addition rate without ultrasonic assistance gave a more compact surface morphology. Gopi et al. [41] reported an approach for particle size reduction using a novel ultrasonic treatment coupled with sol–gel synthesis of nano-HAp powders, as compared to the conventional sol–gel method. Such nano sized HAp powders could be used as coating material for biomedical applications.

Rodrıguez-Lorenzo et al. [42] prepared apatites with different stoichiometries and morphologies using aqueous solutions. Their work showed that it is possible to control stoichiometry, crystallinity, and morphology of calcium phosphate apatites as a function of reaction conditions. Homogenous sets of the final product started with higher concentrations of reagents. Obtaining apatites with crystal size in the range of adult human bone or dentin was done at reaction temperatures in the range 25-37°C, while

higher temperatures ~90°C were necessary to copy apatites with crystal sizes in the range of enamel.

Anandan and Jaiswal [14] synthesized human bone-like HAp using Schiff's base as a surfactant, organic modifier, and a chelator to bring calcium and phosphate precursors together for HAp formation mimicking the mineral in the human bone by synthesizing needle-like HAp nanostructures. They used a Schiff's base derived from salicylaldehyde and 1, 4-diaminobutane as complexing agent/organic modifier to synthesize HAp [43]. SEM photos showed highly crystalline nano-needles of HAp with diameter 10 nm and length 50–60 nm similar to the morphology of HAp in natural human bone [44]. In addition, results obtained from TGA and DSC, even after exposure to higher temperatures, showed only a single phase of HAp. This thermal stability of HAp suggests that it could be incorporated into polymer composites to obtain better biomaterials for biomedical applications.

Nazeer et al. [45] investigated the solvent effect on the synthesis of HAp with a Ca/P ratio of 1.67 through a sol–gel process by reacting Ca and P precursors in different solvent mixtures of distilled water, tetrahydrofuran (THF) and *N*,*N*-dimethylformamide (DMF). These mixtures with different polarities and dielectric constants were used as the reaction media. They performed physical and chemical characterization with FESEM, BET, ATR-FTIR, Raman, XRF and XRD techniques and found that water-based reaction medium with highest dielectric constant yielded mainly β-CPF with a minor amount of HAp. In DMF/water-based synthesis, HAp was obtained as the major phase with a very minor amount of β-CPF. In THF/water solvent system with the lowest dielectric constant, pure HAp was synthesized. Thus, choosing a suitable solvent plays a major

role in synthesizing a near pure single phase of HAp for specific applications such as 3D printing where multi-phase inks might not be favored.

Reaction temperature plays a major role in determining particle size, crystal size, and shape. Specific surface area was found to decrease with the increase of reaction temperature. Longer reaction times lead to apatites with higher Ca/P ratios as well as bigger particle sizes, while shorter times and/or lower temperatures yielded calcium deficient apatite. Atmospheres of N_2 or CO_2 can affect the absorption of impurity ions or CO_3^{2-} groups into the apatitic structure. Aging of the precipitates at room temperature can lead to the incorporation of minor quantities of carbonate from the medium. Ben-Arfa et al. [46] synthesized HAp powders by an aqueous sol-gel method requiring 1h, instead of conventional aging and drying over 1 week (~200 h), that resulted in a similar product with slightly enhanced bioactivity. They also employed a fast-drying process using a rotary evaporator to directly dry the slurry in 1h with no aging. According to Ben-Arfa, this fast drying, a 50-to 200-fold reduction in process time, results in nano powders with smaller crystallite sizes, higher surface areas, reproducible and controlled features, versatility to prepare HAp or biphasic mixtures (HAp + β-TCP) within faster aging/drying time when compared to the conventional drying method. Moreover, the study showed that pH and higher synthesis temperatures are the most relevant factors in determining the crystalline phase and form calcium phosphates with higher Ca:P ratios. This fast-drying method reduced calcination temperatures and thus, eliminated secondary phases of biphasic mixtures (HAp + β-TCP) from the starting apatitic powders. Matto et al. [47] studied the effects of drying methods on the microstructure of biphasic calcium phosphate ceramics (BCP) obtained by sol-gel method. Their point was to prove that

desired apatite phases with singular physical-chemical properties are related to process conditions such as precursor mixtures, aging, drying method, calcination and sintering. BCP powders were synthesized by an alcoholic sol–gel method and dried either in a muffle-furnace at 200°C/2h with heating rate of 5°C/min or freeze-drying (BCP-FD), before calcination. XRD analysis revealed that HAp phase contained in alcoholic sol-gel processed BCP powder underwent partial transformation into β-TCP after sintering, resulting in higher particle reactivity. However, sintered freeze-dried BCP samples remained biphasic from the powder and presented no trace of pyrophosphate phase in the FTIR spectrum. In conclusion, the freeze-drying method produced a powder with better features for preventing partial HAp/β-TCP phase transformation.

c. Hydrothermal technique:

Hydro- and solvo-thermal processing involves the use of a solvent (with precursor soluble ions), which is heated in a sealed vessel. The typical solvent in a hydrothermal synthesis is water that reaches temperatures above its boiling point as the pressure inside the sealed vessel exceeds the ambient pressure [35]. In the last century, hydrothermal techniques were a common method for various ceramic materials including HAp. Hydrothermal synthesis involves single or heterogeneous phase reactions in water conducted at ambient conditions or elevated temperatures (T>25°C) and saturated vapor pressures (P>100 kPa) to crystallize ceramic materials directly from solutions [48]. Upper limits of hydrothermal synthesis extend to over 1000ºC and 500 MPa pressure. However, 350ºC and pressures approximately 50 MPa or less are preferred for commercial processes [49].

The pressure and temperature determine and regulate the reactions, including crystal nucleation, growth, and aging. Crystalline HAp can be produced in one step via hydro- and solvothermal synthesis without requiring post heat treatment [50], but the scalability of these "batch" techniques is limited to the size of the reaction vessel [51]. Furthermore, solvent and surfactant selection may require modification to optimize production.

Bilton et al. [52] compared hydrothermal and sol-gel synthesis methods in preparing nano-particulate HAp powders. Their elemental analysis data and characterization showed that hydrothermal powder had a single phase of near-stoichiometric needle-like HAp nano-particles. Bilton et al. found by studying the Ca/P ratios of each powder using a transmission electron microscope with energy dispersive X-ray spectroscopy (TEM-EDX), that there is a greater compositional variability of particles from the sol-gel route (Ca/P ratio of 1.67, and a small fraction higher than that) compared to the hydrothermal route (average Ca/P ratio of 1.61) with no detection of Ca-rich particles. On the other hand, there was the presence of secondary phases in the sol-gel powders, which was attributed to the evaporative loss of the precursor phosphate phases during specimen preparation and breakdown of the primary HAp phase during calcination. The sol-gel synthesis method produced HAp nano-particles that were a mixture of equiaxed and rod-like particles.

Through intensive research, cost-effective, lower pressure reactors, and chemical methodologies have led to a better understanding of hydrothermal chemistry reducing the reaction time, temperature, and pressure to $T<200^{\circ}C$ and $P<1.5$ MPa [48]. Manafi et al. [53] synthesized HAp by dissolving $HPO_4.2H_2O$ in NaOH and distilled water, followed

by adding 2-3 g cetyl trimethyl ammonium bromide (CTAB). The hydrothermal synthesis was conducted at 150°C for 2 hours in an electric oven. This sono-chemical process resulted in the formation of HAp crystals. The crystallite size and crystallinity degree of the HAp increased with further annealing.

For an effective and precise morphology control of HAp crystals, Neira et al. [54] successfully synthesized HAp powders on a gram scale at low temperature 90°C through a urea-assisted hydrothermal reaction between calcium nitrate tetrahydrate $Ca(NO_3)_2$ $4H_2O$ and di-ammonium hydrogen phosphate $(NH_4)_2HPO_4$ as precursors. The morphology of the HAp crystals was controlled by changing the concentrations of the components and the slow thermal decomposition kinetics of urea. Single-crystal, nearly defect-free microstructures of carbonated hydroxyapatite crystals were obtained in different shapes such as plate-like, hexagonal prism-like, needle-like and fine-plate-like particle morphologies. The shapes and crystallinity were observed with TEM and electron diffraction (ED). The HAp particles obtained in this study showed higher mechanical properties under nanoindentation, and better hardness and elastic moduli due to the crystal orientation.

Ziani et al. [55] worked on doping calculated amounts of magnesium ions (Mg^{+2}) from 0 to 10% (molar ratio) into the calcium sol solution. The structure and morphology of the gels obtained after mixing the phosphorus and (calcium + magnesium) solution were different, and their condensation rates depended on the quantities of magnesium added. Their XRD, FTIR, and ICP results indicated that the magnesium was incorporated into the lattice structure of HAp, while SEM and TEM results confirmed the

influence of Mg on their morphology (needle and irregular shape) and crystallite size, which was about 30–60 nm.

Different morphologies lead to a variety of applications. Xuel et al. [56] synthesized highly crystalline carbonated hydroxyapatite CHA nanorods with different carbonate levels by a convenient hydrothermal reaction. Increasing the carbonate content decreased the nanorod lengths slightly and increased the widths. This change of the carbonate content played a role changing the crystallinity of CHA nanorods. The substitution of CO_3^{2-} ions caused lattice defects that eventually decreased the total crystallinity of the product. However, biocompatibility and osteogenic differentiation tests proved that the CHA nanorods were biological apatites and a promising biomaterial for bone-tissue engineering applications. A main factor to obtain the desired morphology was using a considerable amount of CTAB as a template. TEM micrographs from Wang et al. [57] showed the probable mechanism involving interactions of the tetrahedral CTAB cation structure, the tetrahedral PO_4^{3-} structure and the OH^- ions at different pH values, resulting in HAp in a variety of shapes, from spheroids with a diameter of ~27 nm, achieved at 90°C, pH=13 for 20 h, to long fibers ~1125 nm and a diameter of ~60 nm at 150°C, pH=9 for 20 h. The results showed that the nanosized HAp particles can be tailored through the control of the process temperature, the reaction time, concentration of CTAB, and the pH value of the solution.

2. Doping of HAp

A significant amount of research has been done to enhance properties and applications of HAp synthesized by different methods especially for resorbable scaffolds and coatings. Due to its biocompatibility, chemical similarity to the human bone mineral, particle size, crystal morphology that controls the interfaces with cells, proteins or peptides, hydroxyapatite is an ideal candidate for orthopedic implants, dental implants, and repairing hard tissues [42]. Due to the ionic contamination of biological HAp, much research has focused on the ion doping of HAp structure [58]. Doping ions such as strontium (Sr), magnesium (Mg) and/or, fluorine (F) into HAp structure improves HAp properties for different uses. Sr and Mg hinder the growth of HAp particles and increase their solubility and positive surface charges making HAp a good candidate for gene delivery [59]. On the other hand, fluoride increases the structural order of HAp by preferred binding with OH, and consequently, fluoridated hydroxyapatite (FHAp) has a higher thermal and chemical stability than undoped HAp [60] in addition to greater mechanical properties when sintered at high temperatures. By increasing the fluorine content, Esnaashary et al. [58] found that the sinterability of FHAp samples was decreased and the hardness of FHAp samples was improved.

Most research is directed towards modified synthetic apatites involving the substitution of chemical species found in natural bone. The ability of HAp to exchange Ca^{2+} ions influences crystallinity, physico-chemical and biological properties [61]. Because of the poor mechanical characteristics, mainly its brittleness (K_{Ic} ~ 1-2 MPa $m^{1/2}$), HAp ceramics are mostly limited to applications of low mechanical loads. Remesh et al. [62] studied the effect of manganese (IV) oxide (MnO_2) on the sinterability of HAp.

They reported a beneficial effect of a small amount of (MnO_2) on the process of low-temperature densification of the modified HA material without causing any changes in phase composition. As a result, the mechanical strength of the bioceramics modified in this way increased. Paluszkiewicz et al. [63] showed a clear influence of manganese substitution on the structure and thermal stability of Mn-doped hydroxyapatite. They also showed that the degree of MnHA decomposition depended on the wt% of Mn introduced in the initial powder, in addition to the calcination temperature. Czeslawa stated that the presence of manganese additions in the crystalline structure of HA influenced the adherence of bone cells to the implant material and induced their spread and viability. Mayer et al. [64] related this advantage to the conformational changes of integrins, i.e. a group of receptors, responsible for activation of cell adherence processes, caused by manganese.

Beheri et al. [65] studied the mechanical properties and microstructure of reinforced hydroxyapatite/calcium silicate nano-composites synthesized by both chemical precipitation and a sol–gel method. Their research showed the effect of changing the ratios between HAp and calcium silicate on the mechanical properties, and microstructure, in an in vitro study. They observed that the mechanical properties were improved with increasing the calcium silicate ratio in the composite. In addition, their work confirmed formation and nucleation of apatite on the composite surfaces, which contained a low content of calcium silicate after one week of immersion. According to Beheri, HAp/ calcium silicate composites, containing high HAp content at the expense of calcium silicate content, are promising for bone substitute applications, especially in load bearing sites.

Ruys [66] worked on determining the feasibility of chemically doping HAp with silicon through a metathesis method using $Ca_3(N0_3)_2$, $(NH_4)_2 HP0_4$, and NH_4OH and adding silicon by a sol-gel route using tetraethyl orthosilicate [TEOS] and ethanol up to a Si:HAp molar ratio of 2. His study showed the nucleation and growth of HAp crystals on silicon-rich substrates in addition to calcium silicophosphate, TCP, and phosphosilicate glass. This research identified silicon as a calcifying agent rather than as a resident structural species. Hence, silicon may be used for improvement of bone in-growth rates for bioactive prosthetic materials as long as the dopant levels are kept low in order to keep the TCP content to a minimum and reduce the possibility of biodegradability in-vivo [66].

Sawdi et al. [67] used fluorine to substitute for some of the hydroxyl groups to form fluoridated hydroxyapatite (FHA) [4-6 wt% F, (FHA, $Ca_{10}(PO_4)_6(OH)_2–F_x$]. Fluorinated hydroxyapatite has been developed by different methods to increase strength and give higher corrosion resistance in biofluids and acids reducing the risk of dental caries with the use of pure HAp. The stability of FHA has been improved as the fluoridated hydroxyapatite has a more compact structure than HAp, resulting in decreased dissolution rate, and enhanced adhesion strength between the coating and substrate. The effects of fluoride on bone quality are dependent on the balance between the beneficial effects and deleterious effects [68].

Morais et al. [69] reported the results of doping cerium into a glass-reinforced HAp to study the antibacterial and osteoconductive properties for bone tissue regeneration. The results showed that the Ce inclusion in the glass reinforced-HAp matrix induced the antimicrobial ability of the composite by promoting cell adhesion,

seeding osteoblastic populations, and proliferation. The outcome induced regeneration of the bone tissue.

3. 3D printing of Hydroxyapatite

In general, three-dimensional (3D) printing, also known as additive manufacturing (AM) is a direct fabrication process of parts layer-by-layer guided by a computer-aided design (CAD) program. For biomedical applications and tissue engineering (TE), hydroxyapatite falls into fabrication approaches such as 3D-Bioplotter or Direct Ink Writing, Selective Laser Sintering, and Robotic-Assisted Deposition or Robocasting depending on the end user application [70]. Some key advantages of 3D printing in biomedical applications are that it allows more flexibility regarding manufacturing customized, low-volume, complex implants with functional grading, without the need for high energy and without material waste. 3D printing or AM represents a great opportunity to produce a variety of biomedical devices such as orthopedic implants.

Materials with compositions similar to the mineral phase of bone have high clinical interest [71]. A wide range of bioactive ceramics, such as HAp, (β-TCP, bioactive glass (BG) and calcium silicate (CS), bioactive ceramic scaffolds could react with physiological fluids, resulting in the formation of strong chemical bonding to bone tissues due to the formation of bone-like HA layers [72] and then self-degrade in vivo. Typically, a water-soluble polymer is used as a binder for 3D printing. For example, Seitz et al. [73] reported 3D printing of HAp scaffolds with a polymer-based binder solution layer-by-layer, scaffolds are heated at 400°C to burn out the organic

components, and then rapidly sintered at 1250°C in ambient air. Controlled shapes and pore sizes were fabricated. Pires et al. [74] changed printing parameters and binder proportions when he 3D fabricated and sintered HAp scaffolds. His results showed that increasing sintering temperatures led to a slight increase in density, compressive strength and tangent modulus of the scaffolds with an expected porosity decrease. Furthermore, HAp scaffolds showed superior biocompatibility compared with β-TCP scaffolds and BioOss® scaffolds [74].

Razali et al. [76] studied the effects of excess calcium on the handling and mechanical properties of hydrothermal derived calcium phosphate cement (CPC) for bone filling applications using calcium oxide, CaO and ammonium dihydrogen phosphate, $NH_4H_2PO_4$ as the calcium and phosphorus precursors respectively. The effects of calcium excess were evaluated by varying the CaO content at 0, 5 and 15 mole %. Their work showed that an increase in calcium content of CPC caused poor injectability performance due to lack of water content in the cement and the increase of viscosity as well as the cement self-setting rate. However, agglomerated particles in the CPC may increase the overall strength of the cement [77] and the highest compressive strength achieved by CPC-5 at 1.682 MPa, compared to the compressive strength of CPC-0 and CPC-15 at 1.638 MPa and 1.508 MPa, respectively. The mixture with higher calcium excess is found to be sticky due to the interparticle attractive forces, which hardens the cement faster [78].

Polymer materials that are currently used for 3D printing for biomedical applications are based on naturally derived polymers (gelatin, alginate, and collagen) or synthetic polymer molecules such as polyethylene glycol (PEG), poly lactic-co-glycolic

acid (PLGA), and polyvinyl alcohol (PVA). For such applications, printable materials should have several desired characters, e.g., printability, biocompatibility, good mechanical properties and structural properties [79]. It is essential for any successful transplantation to have a decent interaction with endogamous tissues [80]. 3D printing has addressed this problem by allowing the control of pore size and pore distribution in the scaffold [81]. Printing of composite scaffolds with high biocompatibility was achieved by adding bioactive particles into polymer. The biodegradable and biocompatible polymers maintain the toughness of the printed scaffold, while the brittle biomaterial particles increase biocompatibility.

Synthetic calcium phosphates such as HAp [82] and TCP [84] have been widely applied in tissue engineering to fabricate biocompatible composite scaffolds through variable 3D printing technologies. These materials effectively generate nano/microscale topology in composite scaffolds and greatly improve the hydrophilicity of the scaffolds, thus increase the bioactivity of scaffolds [79]. To improve the strength of scaffolds, most of the composite scaffolds were prepared by blending HAp or TCP with polymer matrix. Xia et al. [84] selected HAp as reinforcement and fabricated a poly caprolactone (PCL) based scaffold by SLS technique. A 130% improvement in the compressive strength of fabricated composite scaffolds was demonstrated.

When it comes to the 3D fabrication of an artificial bone scaffold process, the interaction mechanism between binder and bioceramic powder determines the microstructure and macro mechanical properties of HAp bone scaffold. Wei et al. [85] explained in their work that ionic bonds and hydrogen bonds are formed between the polar functional groups in the binder polymer and the Ca, and –OH groups in HAp. They

also stated that Young's modulus of bone scaffolds is limited by the Young's modulus of binders, and the compressive strength is mainly decided by the viscosity of the binders. Moreover, the porosities within HAp pellets and the incomplete infiltration of binder in the HAp surface are the main reasons for the differences in mechanical properties.

The core challenges associated with biomedical 3D printing are in achieving high mechanical properties, durability, and designed architectures that satisfy both mechanical and functional requirements especially in load-bearing implants. The challenges go further in the ability of 3D printing technologies to accurately produce desired porous architectures that meet design objectives due to the resolution capability of the 3D printer in use. Implant pores can be infiltrated with polymers to modify strength, fracture resistance, and biodegradation speed. Micro-porosity is vital for fluid exchange and cellular influx during bone healing.

HAp has been infiltrated with non-degradable methacrylate polymers improving the bending strength of 3D printed HAp ceramics by nearly two orders of magnitude, to >50 MPa [70,86]. Surface roughness of the product plays a critical role to induce cell anchoring, proliferation and integration, but at the same time for other cases this roughness might be unfavorable because of stimulating foreign body reactions or releasing particles around the implant [70].

The size and shape of pores of granular HAp used in 3D printing can affect vascularization. New bone formation requires a critical pore size (>350 μ) for better cell migration and angiogenesis in vivo [86]. For such accurate fabrication, porogen leaching, electrospun matrices, and micromolding techniques are now in use. Optimizing pore size becomes essential for molecular signaling, nutrition supply, waste removal, and

tissue studies in vitro and in vivo. Weia et al. [86] investigated new nano-hydroxyapatite (NHAp)/polymer composite scaffolds with high porosity (90% and above) developed using thermally induced phase separation techniques. Nano-sized HAp particles were effectively incorporated into the porous scaffold and improved the mechanical properties and protein adsorption of the composite scaffolds, while maintaining high porosity and suitable micro architecture. The results suggest that the newly developed nano-HAp/polymer composite scaffolds may serve as an excellent 3D substrate for cell attachment and migration in bone tissue engineering.

Suwanprateeb et al. [89] studied the mechanical properties and bioactivity of a 3D printed hydroxyapatite composite infused with bisphenol A glycidyl methacrylate resin (HAp/bis-GMA). As-fabricated green 3DP samples and 1300°C sintered 3DP samples were studied. The HAp volume fraction in both composites was found to be 0.22 and 0.36, which are typical levels that could show bioactivity without compromising the mechanical properties. It was found that both 3DP composites had higher flexural modulus, strength and strain-at-fracture than the initial 3DP hydroxyapatite sample. However, in contrast, the sintered composite had a higher HAp content, higher density and greater modulus, but lower strength and strain-at-fracture than the composite produced from green 3DP sample. In vitro toxicity showed that 3DP samples of HAp/bis-GMA based composites were non-toxic and the higher content of HAp helped more osteoblast cells to attach and attain normal morphology on the surface of composites. Poor interfacial bonding between the HAp and matrix resin was observed in both composites, which explains average bioactivity for the greater amount of HAp in the composite.

In another HAp composite study, Sarsilmaz et al. [88] investigated a composite implant of HAp and polyethylene (PE) for the usability in large bone defects and orthopedic surgery in mongrel dogs. The implants were manufactured in blocks by hot compacting the mixture of 80% HAp and 20% PE weight ratio. Polyethylene being a bioinert material required that the surface of the implant had to be as reactive as possible with the neighboring tissues by adding the greatest possible amount of HAp and maintaining a rough outer surface to increase cell proliferation and adhesion. The study found that the mechanical properties of the implant were close to those of the human cortical bone, except the Poisson's ratio, and the composite was considered bioabsorbable due to light inflammation by the penetration of osteoid tissue into the implant, especially with higher %HAp and surface pores.

Chumnanklang et al. [89] studied the influence of binder concentration in the slurry for pre-coated particles on the properties of a hydroxyapatite part fabricated by 3DP. The demonstration was done by using maltodextrin, a low-cost water-soluble natural polysaccharide binder, and a spray drying technique to prepare the raw material. The concentration of binder was found to influence properties of both green and sintered parts. Eventually, increasing the binder concentration and pre-coated particle size increased the green strength of the sintered HAp samples. The researchers stated that it is likely that a large pre-coated particle would yield a stronger 3DP hydroxyapatite part because of the better densification of intra-particles than inter-particles during the sintering process.

Micro-nozzle 3D printing for direct biomaterial ink deposition is a promising method to print microscale features [90]. A variety of materials including poly (2-

hydroxyethyl methacrylate) (pHEMA), polyacrylic acid, (PAA), polyethylenimine (PEI) have been used as ink solution in the direct writing technique [91]. Sun et al. [91] investigated the effect of direct writing architectures on cell composition and human tissue formation. Biomaterial architecture, including pore size and shape, has a huge impact on bone tissue engineering from various materials. They worked on 3D silk/HAp scaffolds that were used to support the growth of co-cultures of human bone marrow-derived mesenchymal stem cells (hMSCs) and found the spacing between silk/HAp filaments is approximately 400 μ, the vascular-like structures follow the scaffold morphology.

Michnaa et al. [92] studied the effects of calcining and milling on as received HAp powder to formulate ink for direct-writing assembly. Upon calcining at 1100°C for 10 h, there was a dramatic change in powder morphology yielding a final specific surface area (SSA) value of 3.8 m^2/g after a starting value of 75.7m^2/g. The optimal powder morphology emerged only after calcining at this temperature for several hours. Longer calcination times are required for the particles to adopt the nominally smooth, pore-free morphology. They found as well that concentrated HAp inks suitable for direct-write assembly of 3D periodic scaffolds require both a high solid loading (~45 vol%) and high elastic shear modulus (~10^5 Pa). The HAp inks used in their work were mainly prepared by making a stable colloidal suspension (30 vol% HAp) in deionized water with an appropriate amount of PAA dispersant (0.57mg PAA/m^2 HAp) and an adjusted pH of 9 followed by ultrasonication. Viscosifier and defoamer were then added in the appropriate amounts, followed by shaking on a paint shaker and addition of PEI gelling agent.

3D powder printing and 3D plotting are considered appropriate methods for processing of calcium phosphate-based materials [93]. Mechanical properties (e.g. compressive strength) can be improved by sintering as a post-processing step. Kumar et al. [94] studied chemical stabilization and structural properties of 3D scaffolds and the comparison in cases of alginate cross-linking versus sintering. For extrusion method of 3D plotting, two different binders, maltodextrin and sodium alginate (cross-linked with $CaCl_2$ solution), were used to fabricate scaffolds with parallelepiped porous architectures having up to 74% porosity. Sintered scaffolds exhibited progressive deformation and delayed fracture under external loading. The study showed hydroxyapatite–alginate scaffolds having a higher compressive strength (9.5 ± 0.5 MPa) than hydroxyapatite–maltodextrin scaffolds (7.0 ± 0.6 MPa) due to differences in microstructure. After sintering and complete removal of polymeric phase, a pure inorganic, micro-porous 3D structure remained. Holding at 450°C for 30 min, and heating at 1250°C for 1 h lead to densification and 30% decrease in total microporosity. In contrast, the sintering of HAp–alginate samples at 1250°C for 1 h lead to the complete transformation of HAp to chlorapatite. In 3D powder printing, the choice of binder is limited depending on the powder composition [95]. The crystallinity of HAp determines its stability in body fluids at physiological pH where low crystallinity HAp with porous architecture is recommended for faster bone regeneration [96].

4. **Sintering Hydroxyapatite and Calcium Phosphates**

The low chemical and thermal stability of HAp in general, affects its sinterability leading to poor mechanical properties of a HAp bulk [58]. Therefore, poor sinterability

has restricted HAp applications to non-load bearing conditions such as coatings or combinations with other materials. However, poor sinterability does not degrade the hardness of HAp, as Esnaashary et al. [58] have shown. In addition, lower sintering temperature reduces material processing cost and prevents second phase decomposition at high temperatures [97,98].

Ghosh and Sarkar [99] studied the effect of preparation on the microstructural properties and microhardness of sintered HAp samples synthesized by three different routes: wet chemical precipitation (HCop), sol–gel (HSol), and solution combustion (HCom) methods. The calcined powders had higher particle size for HCop than either HSol or HCom powders. Powder particles grew from nano- to micro-range sizes as the calcination temperature increased from 700 to 1000°C. The HAp synthesized by the wet chemical precipitation had the highest microhardness value and bulk density due to the very high compact grain structure with almost no porosity. The hardness was lower for the samples (HCom, HSol) sintered at 1200°C because of the lower bulk density value at this temperature [100] making them more suitable for load bearing applications.

Customizing sintering schedules can help in designing the final required properties of a bioceramic by altering the microstructure, shape and size of the grain, composition, and surface chemistry [101]. The sintering characteristics are dependent on the surface area of the powder, heating rate, Ca/P ratio and the mode of heating. Usually, the objective is to increase the surface area and prevent grain growth. Whatever the sintering technique may be, grain growth occurs mainly during the last step of sintering, when the relative bulk density reaches 95% of the maximum value. [102]

HAp powders were reported to reach theoretical density by pressureless sintering [103] at 1000-1200°C. When the sintering/holding temperature exceeds 1300°C, HAp is unstable leading to grain growth and decomposition. The processing of HAp under vacuum leads to the decomposition of HAp, while processing under high partial pressure of water prevents decomposition [101]. Meanwhile, the presence of water in the sintering atmosphere constrains densification of HAp and accelerates the grain growth [104]. The densification of HAp attains a saturation limit between 1100 and 1300°C.

Sintering of HAp is difficult due to the presence of OH content, which decomposes to form TCP and anhydrous calcium phosphates at ~1200-1450°C. Dehydroxylation leads to decomposition, and this -OH ion loss can be reversed during cooling to ambient temperature [105]. Partial dehydration of HA into oxy-hydroxyapatite may occur [106, 107] according to a reversible reaction:

$$Ca_{10}(PO_4)_6(OH)_2 \leftrightarrow Ca_{10}(PO_4)_6(OH)_{2-2y}O_y + yH_2O\ (gas) \ldots \quad \text{eq (2)}$$

In general, dehydroxylation tends to occur at temperatures >800°C and accelerates up to 1350°C. At a temperature >1350°C, irreversible dehydroxylation accompanied by decomposition occurs, whereas densification at a temperature >900°C takes place depending on the type of powder used. The densification saturates at ~1150–1200°C with closed porosity. Through the progress of the dehydroxylation, vacancies enhance both grain coalescence in the first stage of sintering at low temperatures and densification during the intermediate stage at higher temperatures. Dehydroxylation can prevent densification at the final stage of sintering when the pores are closed, and trapped water vapor is present [102]. Sintering is delayed by moisture [108]. Substituted ions may also play a role in the ability to sinter. At the microscopic scale, ionic substitutions

in hydroxyapatite create lattice defects/point defects that modify the sintering rate. They can either accelerate or slow down the sintering rate. Still, and despite the composition of CaP, the transition point between densification and favoring grain growth occurs at ~95% of relative bulk density [102]. Grain growth and densification processes occur simultaneously to some degree, but grain growth is particularly active during the last stage of sintering at high temperatures.

Grain growth and the probability of chemical decomposition are some of the problems encountered during conventional sintering [109]. Esnaashary applied a two-step sintering method by Chen and Wang [110] to achieve nanostructural properties for his prepared HAp. In two-step sintering, the sample was heated up to a temperature sufficiently high to reach a critical relative bulk density of ~70%. Then, it is rapidly cooled and held at a lower temperature until densification is completed [111]. Grain boundary migration is hindered by triple grain junctions, which form at higher temperatures in the first step and become stable by densification through volume and grain boundary diffusion at lower temperatures in the second step [112]. The critical element in the first step is achieving an initial relative density of more than 75% to render pores unstable and to form triple grain junctions [58, 112]. Lastly, to achieve lower sintering temperatures with higher densification rates, several sintering techniques in controlled atmospheres, flash sintering, spark plasma sintering (SPS), and hot isostatic pressing (HIP) have been used on HAp [101, 102].

Chapter Three

Materials and Methods

Introduction

Over the past forty years, there has been much research and success in synthesizing new ceramic materials at low temperatures. Sol-gel processing, because of its atomic level mixing in solutions, has an advantage in synthesizing highly reactive starting materials of many ceramic composition [49]. Meanwhile, hydrothermal processing is popular for crystalline phases using modest temperatures in high-pressure water vessels [49]. In this thesis, these synthesis methods are the basis for producing fine powders with controlled size, composition, and purity. Powders prepared by these methods were compared to a powder that is commercially available. In total, three powders were examined.

3.1 Sol-Gel preparation of Hydroxyapatite [112]

First, a sol–gel synthesis was used to obtain the hydroxyapatite nano powder. The flowchart given in Fig.3.1 outlines the experimental procedure used to generate the nano-HAp. In the synthesis, calcium nitrate tetrahydrate $Ca(NO_3)_2.4H_2O$ (Merck) and ammonium dihydrogen phosphate (ADP) $NH_4H_2PO_4$ (Sigma Aldrich) were used as starting Ca and P precursors. Ammonium hydroxide NH_4OH was used to adjust the pH of the solution. The following synthesis reaction was carried out:

$$10Ca(NO_3)_2.4H_2O(s) + 6NH_4H_2PO_4(s) + 14NH_4^+(aq) + OH^-(aq) \rightarrow$$

$$Ca_{10}(PO_4)_6(OH)_2(s) + 20NH_4^+(aq) + 20NO_3^-(aq) + 52H_2O(l) \quad \text{(eq) 3}$$

1.67 M $Ca(NO_3)_2.4H_2O$ solution in ethanol (pH 10) was added to the 1M $NH_4H_2PO_4$ solution (Ca/P=1.67) under vigorous stirring for 20 min at room temperature. After a white milky solution was obtained, it was aged for 24 h at room temperature. The gel obtained after this process was filtered and washed repeatedly using double distilled water to remove $NH_4^+(aq)$ and $NO_3^-(aq)$. In addition, the gel was washed repeatedly using pure acetone (99.8% Merck) to change the phase while preventing agglomeration. The filter cake obtained by this process was then dried at 80°C for 18 h in an oven, and the dried powder was calcined at 750°C for 4 h, using an electric furnace, employing a heating rate of 15°C min^{-1} in air. The final powder was hand crushed in a mortar and pestle.

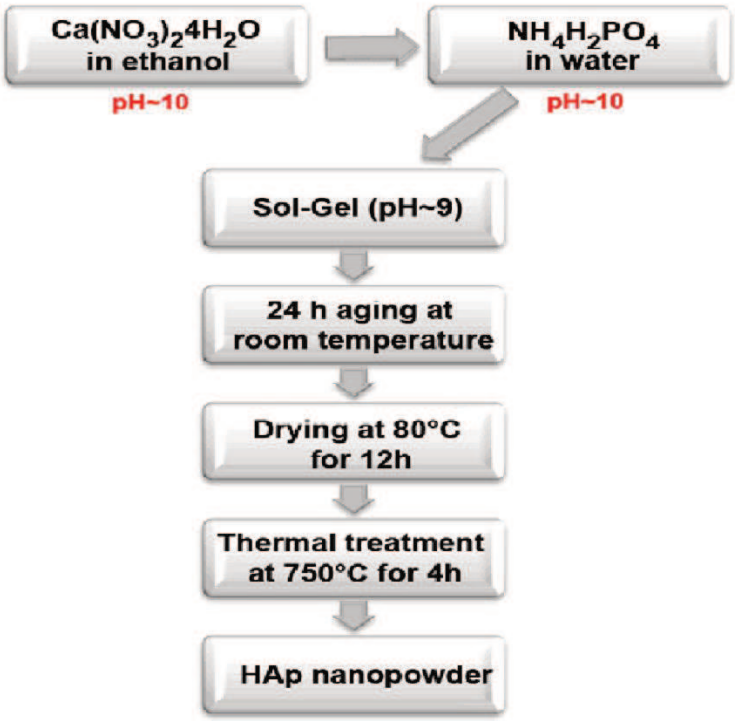

Fig.3.1. The flow chart of HAp preparation.

3.2 Hydrothermal preparation of Hydroxyapatite [113].

The starting materials used in this work were 1 M calcium nitrate tetrahydrate $Ca(NO_3)_2 \cdot 4H_2O$, diammonium hydrogen phosphate$(NH_4)_2HPO_4$, cetyltrimethylammonium bromide (CTAB) and deionized water (≥18.2MΩ). All chemicals were analytical grade, and aqueous solutions were made dissolving them in equal volumes of (75 ml) of deionized water. All mixing was done with continuous and gentle magnetic stirring of 400 rpm and a constant temperature of 90°C. The sample preparation solution had a Ca/P ratio equal to 1.67 (stoichiometric ratio of HA). The

general procedure was the following: 0.67 mol $(NH_4)_2HPO_4$, and 0.025 mol CTAB were dissolved completely in 75 ml of deionized water heated to 90°C, and the pH value was adjusted to 9.3 by adding NH_4OH solution (1 M) for 20 min. At the same time, $Ca(NO_3)_2.4H_2O$ was dissolved in 75ml of deionized water at 90°C and the pH value was also adjusted to 9.3 by adding NH_4OH solution (1 M) for 20 min. Then the $(NH_4)_2HPO_4$/CTAB solution was added slowly drop-wise by burette to the solution of the $Ca(NO_3)_2.4H_2O$. The final milky suspension was formed after the pH went above 2.59. The pH was adjusted to pH 10.3 by adding more NH_4OH. The pH adjusted solution was left for vigorous mixing for 45min at 90°C and 1000 rpm to ensure the reacting and complexing was completed. Then, the mixture was transferred to a 250ml Teflon vessel sealed tightly and heated in an oven at 150°C for 24 h. The precipitate was then rinsed to discard the extra solution and then double washed with deionized water to change the phase, filtered, washed again with methanol (Sigma Aldrich 99.8%) and filtered to remove the residual CTAB and nitrate ions. A gel-like paste was produced which was then dried at 100°C for 24 h to yield white powders.

3.3 Commercial Hydroxyapatite.

This sample was provided by FLUIDINOVA, S.A a spin-off from the Faculty of Engineering at the University of Porto (Portugal) 2005. FLUIDINOVA is a specialized manufacturer and supplier of synthetic nano-hydroxyapatite and tricalcium phosphate materials marketed as nanoXIM. The high-quality standards of their products aim at providing companies around the world that operate in the industries of medical devices, oral care, food and a vast number of applications. The company implemented a Quality

Management System and is certified according to ISO-9001 standards in the scope of production of calcium phosphate nanoparticles and hydroxyapatite. The product provided is nanoXIM HAp203, a white powder with 100% phase purity of HAp and particle size distribution (d50) of 10.0 ± 2.0µm. The company states their product has a high BET specific surface area (>100 m^2/g) due to its high porosity conferred by the nanostructure of the hydroxyapatite.

According to the company literature, FLUIDINOVA invented a reproducible process of micromixing and quality control of calcium phosphates nanoparticles synthesized by a wet chemical precipitation method. A static mixer, NETmix® reactor fed by a calcium solution, a phosphorus solution, and an alkaline solution with optional use of a solvent or a surfactant agent was used to synthesize the nanoXIM HAp203. This process performs a great mixing quality at the molecular level to produce particles with nanometric structure, high purity and controlled crystallinity, and controlled crystal size and morphology. This invention also allows programming the reactants injection scheme with a given distribution at the inlet and along the reactor, which enables to program the pH of the reactant media along the reactor.

3.4 Materials characterization

To achieve a comparison study of the three as-synthesized HAp powders, certain information was required to determine the characteristics and properties of the powders. These are phase identification and X-ray diffraction analysis, microstructure, surface area and topography, particle size, thermal properties, and chemical composition. These

comparisons are just the beginning. Further studies under different atmospheres and thermal conditions will be needed to fully understand the properties of the material and their behavior when applied in 3D printing.

Thermogravimetric analysis (TGA) and differential scanning calorimetry (DSC) were used to measure the thermal properties of the powders. A field emission scanning microscope (FESEM) was used to study the surface morphology of the powders. The molecular components and species were identified using Fourier transform infrared spectroscopy (FTIR). BET surface area and pore size distribution were measured to understand the particle sizes within each synthesized powder.

3.4.1 Phase identification and X-ray Diffraction Analysis

Powder XRD patterns were collected at room temperature, using a PANalytical X'Pert Pro diffractometer (Westborough, MA) with a Cu Kα = 1.5406 Å radiation source operating at 45 kV and 40 mA. The diffraction patterns were collected over a 2θ range from 5° to 90° with an incremental step size of 0.04° using flat plane geometry. The acquisition time was set at 32.895 seconds for each scan and a step size of 0.0131303°. The powder XRD pattern was used to confirm the phase of the final HAp powders and to identify any other phases that were present.

3.4.2 Microstructure and FESEM microscopy

A Zeiss Sigma Field Emission Scanning Electron Microscope (FESEM, Thornwood, NY) with full digital image collection was used to investigate the size and morphology of the HAp powders. The importance of determining the morphology is due

to the influence of morphology on the functional properties of HAp and its desired applications.

3.4.3 Fourier Transform Infrared Spectroscopy (FTIR)

Fourier transform infrared spectroscopy (FTIR) is a form of vibrational spectroscopy that relies on the absorbance, transmittance or reflectance of infrared light. Using this method, light is absorbed in different amounts in a sample at distinct frequencies corresponding to the vibrational frequencies of the bonds in the sample. The IR spectra of the samples prepared were recorded in the 4000–400 cm^{-1} range using Perkin-Elmer Frontier™ FTIR spectrophotometer with a UTAR that operates in that mid –IR region (2.5μm-25μm).

3.4.4 Thermogravimetric (TGA) Analysis and Differential Scanning Calorimetry (DSC)

Thermal analysis has been carried out to investigate the thermal stability of the as-synthesized powders. Thermogravimetric analysis (TGA) is a technique in which the substance mass is monitored as a function of temperature or time while subjected to a controlled temperature program in a controlled atmosphere. Differential scanning calorimetry (DSC) is a thermal analysis technique that measures the temperature and heat flow associated with transitions in materials as a function of temperature and time. Such measurements provide quantitative and qualitative information about physical and chemical changes that include endothermic/exothermic processes or changes in heat capacity.

A Netzsch STA 449F5 Jupiter (Burlington, MA) Simultaneous Thermal Analyzer was used to study the thermal behavior of the HAp powders, such as the energy liberated, reaction types exothermic or endothermic, and weight loss of the samples by recording the samples starting weights and heat flow. Thermogravimetric analysis (TG) was conducted on the as-synthesized HAp powders in both air and N_2 with 10°C/min heating rate from room temperature up to 1200°C. This method was used to determine the phase stability and reaction temperatures of the HAp powders.

3.4.5 Brunauer-Emmett-Teller (BET) Surface Area

Particle shape and size affect the densification, sinterability, as well as solubility of HAp for implant applications. Nanosized HAp possesses higher surface area and surface roughness, thereby resulting in better cell adhesion and bone regeneration [7, 114]. The Brunauer-Emmett-Teller (BET) surface area measurements of the HAp powders were carried out using Micromeritics TriStar-3000 (Micromeritics Instrument Corp. GA, USA). The adsorption technique used nitrogen gas to carry out the surface area measurement. Results are presented in tables using the ISO 9277 standard for calculating the specific surface area of solids based on the BET method [114].

3.4.6 Average Particle Size Distribution

Samples were tested using the Mastersizer 3000 Ver. 3.50 (Malvern Instruments Ltd. Malvern, UK) operating in a size range 0.01 - 3500µm dispersed in DI-water to obtain the average particle size and distribution.

Chapter Four

Results and Discussion

4.1 Phase identification and X-ray Diffraction Analysis

Pressed samples of powder were sintered to temperatures 400, 600, 850, and 1200°C. After the samples cooled to room temperature, X-ray diffraction patterns were collected from samples to identify phases. By knowing the phases that existed after these treatments, it was possible to study phase transformations and decomposition reactions related to the sintering temperature. It was found that the decomposition temperature for HAp was strongly dependent on the particle characteristics and synthesis route [115].

XRD patterns (intensity of diffracted X-rays as a function of 2θ) indicate that all of the synthesized samples are composed of several types of Calcium Phosphates. The sharp peaks confirm they were highly crystalline, whereas broader peaks translate to a higher value of full width at half maximum (FWHM), which indicates smaller size of the crystallites/particles in the powder. The as-synthesized HAp powders did not show any major differences in the diffraction patterns even after increasing the sintering temperatures. The XRD patterns revealed that the sintering process promoted both crystallite growth and enhancement of crystallinity. The main crystallite indices (hkl) from the highest intensity peaks and lattice parameters for all powders are listed in table 4.1. The change in crystallite sizes due to different higher sintering temperatures are shown in table 4.2.

The calculation was done so that a comparison could be made between the crystallite size of the synthesized HAp powders and the growth in the crystallite size with increasing sintering

temperature. The crystalline size, t(hkl), for the pure and sintered HAp powders was calculated using the Debye-Scherrer equation [116,117].

$$t(hkl) = \frac{0.9\lambda}{B\ cos\theta(hkl)} \quad \ldots\ldots \qquad \text{(eq) 4}$$

where, λ is the wavelength of the monochromatic X-ray beam, *B* is the Full Width at Half Maximum (FWHM) of the peak at the maximum intensity, θ(hkl) is the peak diffraction angle that satisfies Bragg's law for each of the (h k l) planes and t(hkl) is the crystallite size.

Regarding the phase composition and purity, all XRD patterns showed that no unexpected elements were involved in any of the reaction syntheses due to the nature of the raw materials used as precursors in the sol-gel process, eq (3), or in the hydrothermal technique. No CaO was observed in any of the X-Ray patterns which indicates a very small amount of HAp carbonation, or no carbonation at all during the synthesis. CaO phase has been shown to have negative effects on the growth of bone cells [118,119].

Among the calcium phosphates formed in the samples, sol-gel powders showed sharp peaks of HAp $Ca_5(PO_4)_3OH$ presented in PDF card (97-005-0656), PDF card (97-000-2633), and PDF card (97-018-4779) as the most dominating phosphates in the sample. Few other phosphates peaks indicated Whitlockite $Ca_{2.99}H_{0.006}(PO_4)_2$ PDF card (97-000-6191), Tricalcium Bis(orthophosphate) $Ca_3(PO_4)_2$ PDF card (97-041-0782), and a peak of calcium dihydride CaH_2 PDF card (97-026-0873). After raising sintering temperatures up to 1200°C, the sol-gel powder showed more matching peaks of HAp, $Ca_{10}(PO_4)_6(OH)_2$ PDF card (97-001-6742) with very few traces of calcium dihydrogen phosphate $Ca(H_2PO_4)_2$ PDF card (97-000-2633).

It is clear that sintering promoted crystal growth at temperatures above 400°C as the diffraction peaks got sharper and no other phases could be detected Table 4.2. Fig.4.1, shows the XRD Pattern for Sol-Gel HAp Powder sintered 400-1200℃.

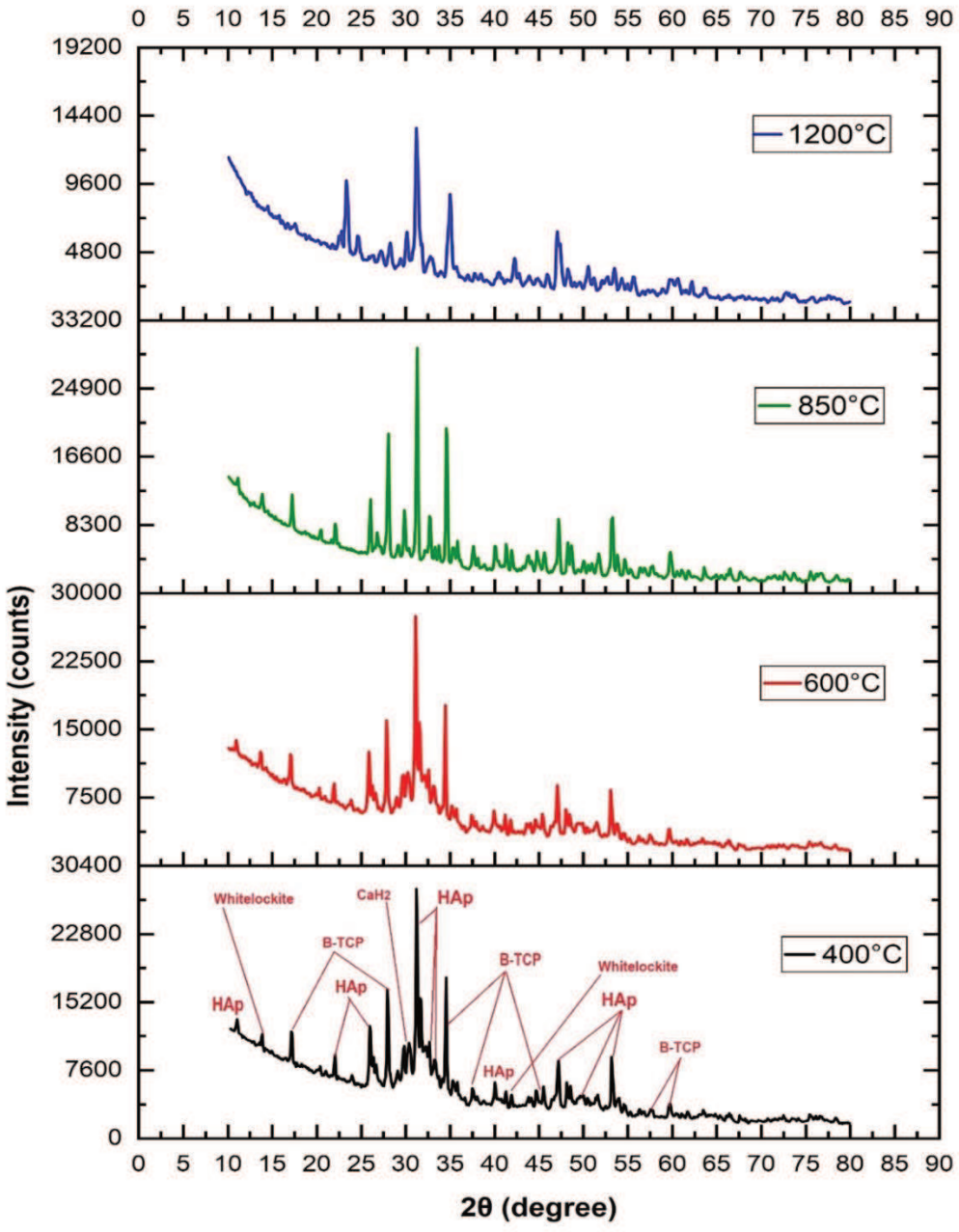

Fig.4.1. XRD Pattern for Sol-Gel HAp Powder sintered 400-1200℃

Table 4.1 Crystallite indices of the calcium phosphates and apatite powders after sintering.

Sintering Temp.	**Sol-gel** (hkl) Indices	**Hydrothermal** (hkl) Indices	**Commercial** (hkl) Indices
400℃	(012) (104) (024) (010) (012) (210) (220) (100) (016) (404) (238) (110) (111) (121) (200) (211) (212) (130) (222) (132) (213) (252) (124) (222)	(100) (200) (002) (120) (012) (112) (211) (300) (130) (132) (213) (321) (402) (202) (301) (131) (310) (311) (103) (222) (312) (123) (232) (140) (420) (144) (511) (322) (502) (152) (210) (110) (212)	(100) (200) (002) (101) (120) (121) (113) (130) (112) (201) (310) (311) (231) (132) (300) (211) (123) (401) (222) (140) (502) (301) (303)
600℃	(210) (214) (110) (128) (220) (012) (112) (211) (226) (016) (404) (010) (020) (024) (120) (104) (300) (202) (100)	(100) (200) (110) (111) (211) (112) (002) (300) (202) (301) (222) (110) (210) (213) (402) (102) (212) (302) (400) (132) (131) (240) (421) (502) (152) (431) (243) (144) (252) (321)	(100) (101) (110) (200) (002) (102) (120) (300) (121) (202) (112) (310) (222) (123) (231) (301) (122) (311) (312) 004) (410) (151) (522) (153) (130) (213) (321) (502)
850℃	(002) (300) (202) (214) (210) (220) (128) (020) (110) (024) (010) (300) (128) (020) (112) (211) (012) (104) (122) (226) (404) (216) (502) (143)	(100) (111) (120) (211) (102) (101) (200) (300) (121) (112) (002) (212) (202) (310) (222) (123) (201) (004) (122) (214) (151) (132) (213) (231) (140) (312) (125) (502) (311) (522) (143) (113)	(100) (200) (120) (121) (300) (112) (002) (202) (222) (310) (211) (130) (123) (231) (502) (102) (210) (301) (212) (131) (321) (412) (014) (332) (240) (203)
1200℃	(100) (012) (006) (110) (024) (128) (226) (238) (132) !131) (502) (511) (144) (301) (211) (201) (220) (310) (402) (213) (210) (112) (321)	(200) (111) (211) (102) (211) (112) (300) (222) (130) (210) (002) (132) (213) (140) (402) (004) (202) (301) (212) (131) (113) (332) (124) (502) (502) (431) (144) (252)	(300) (112) (211) (213) (202) (132) (121) (111) (301) (212) (130) (131) (113) (321) (303) (210) (310) (222) (123) (231) (004) (402) (200) (002) (102)

Table 4.2. The change in crystallite sizes due to different higher sintering temperatures.

Powder sample	Sintering Temp.	Average crystallite size (nm)
Sol-gel	400℃	34.31
	600℃	37.51
	850℃	51.46
	1200℃	55.58
Hydrothermal	400℃	29.24
	600℃	32.97
	850℃	39.34
	1200℃	44.12
Commercial	400℃	15.10
	600℃	23.26
	850℃	40.85
	1200℃	61.25

The hydrothermal powders at 400°C showed phases of HAp as $Ca_{10}(PO_4)_6(OH)_2$ PDF card (97-001-6742) and $Ca_5(PO_4)_3OH$ PDF card (97-015-1414) besides Portlandite $Ca(OH)_2$ PDF card (97-001-5471) in addition to traces of calcium dihydrogen phosphate $Ca(H_2PO_4)_2$ PDF card (97-000-2633). The XRD analysis for powders sintered at 600-1200°C confirmed further formation of HAp represented by different PDF cards in addition to smaller peaks of apatite CaOH β type Na_2CO_3 doped PDF card (97-009-3529) and penta calcium triphosphate V hydroxide $Ca(PO_4)_3OH$, PDF card (97-005-1683).

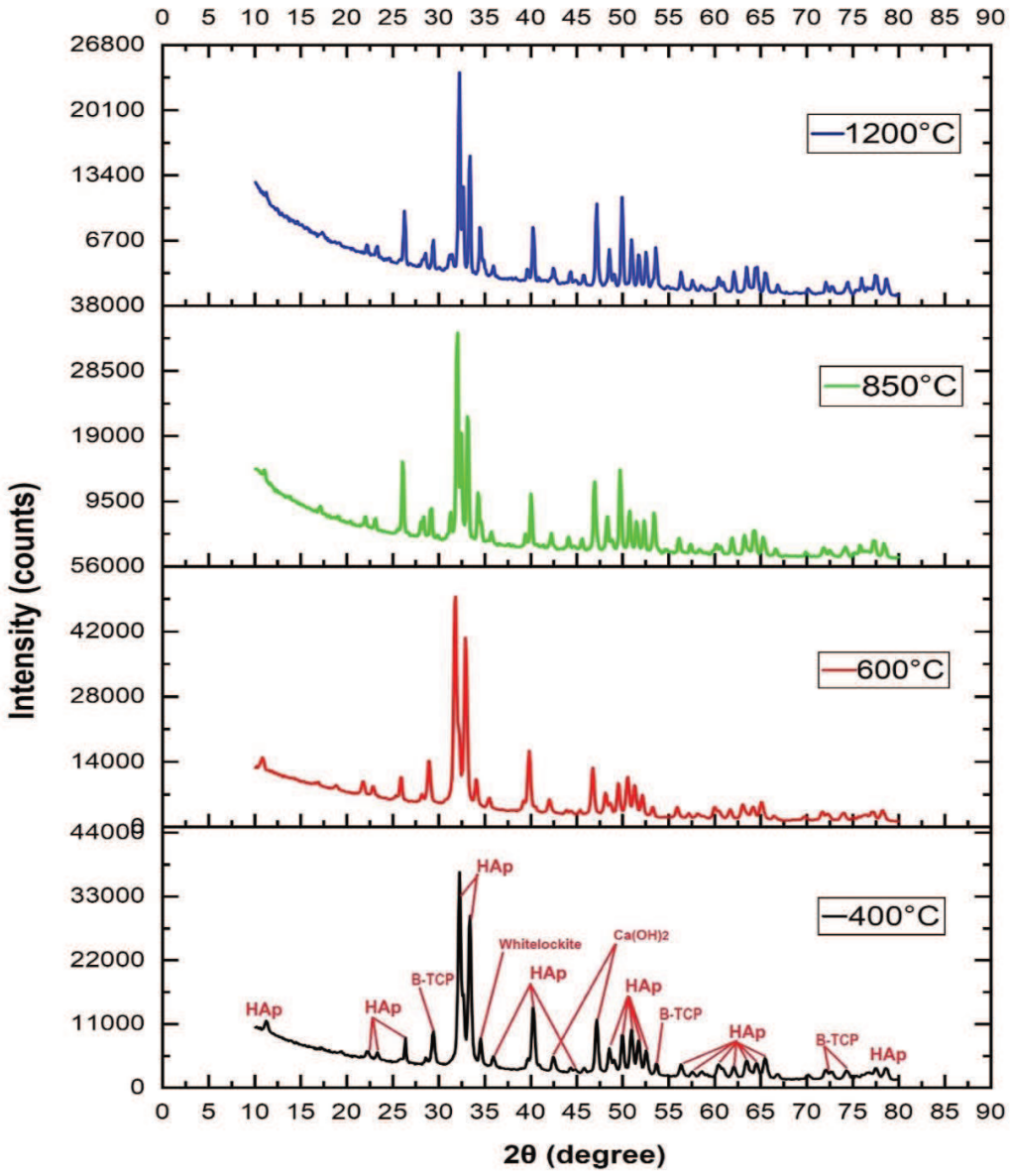

Fig.4.2 XRD Patterns for Hydrothermal HAp Powder sintered 400-1200℃

The diffraction patterns showed a larger number of apatite peaks in comparison to the powders synthesized by the sol-gel route and the commercial powder. Increasing sintering temperatures reflected a stable number of those crystallite sites without showing a dramatic

change in the peak sharpness. This might indicate less crystal growth upon increasing sintering temperatures. Both hydrothermal and commercial powders show generally sharper peaks of apatites than the sol-gel powder, which is consistent with the larger particle size and high degree of crystallinity as observed by FESEM (fig.4.4. a-g). Powders possessing higher crystallinity have the capacity to yield higher counts of Osteoblast cell viability in a 3D scaffold for bone replacements [120]. Hydrothermal HAp sample showed more diffraction peaks of high crystalline HAp at all sintering temperatures. This sample would be very phase stable when it comes to higher sintering temperatures when needed for a final 3D printed scaffold or for bioactive coating. [120].

XRD analysis of the commercial HAp powder is shown in Figure 4.3., which shows major phases of hydroxyapatite $Ca_5(PO_4)_3OH$ PDF card (97-016-1328), PDF card (97-020-3027) and $Ca_{10}(PO_4)_6(OH)_2$ PDF card (97-002-6204). In addition to a few other peaks of apatite CaOH β type Na_2CO_3 doped PDF card (97-009-3529) and penta calcium triphosphate V hydroxide $Ca(PO_4)_3OH$, PDF card (97-005-1683). At the same values of 2θ, the diffraction pattern shows its main peaks over different sintering temperatures. Yet, sintering at 1200°C showed a match of whitlockite $Ca_{2.99}H_{0.006}(PO_4)_2$ PDF card (97-000-6191). As sintering temperatures increase, the crystallite sites get larger which are indicated by sharper diffraction peaks associated with high intensities (fig 4.3).

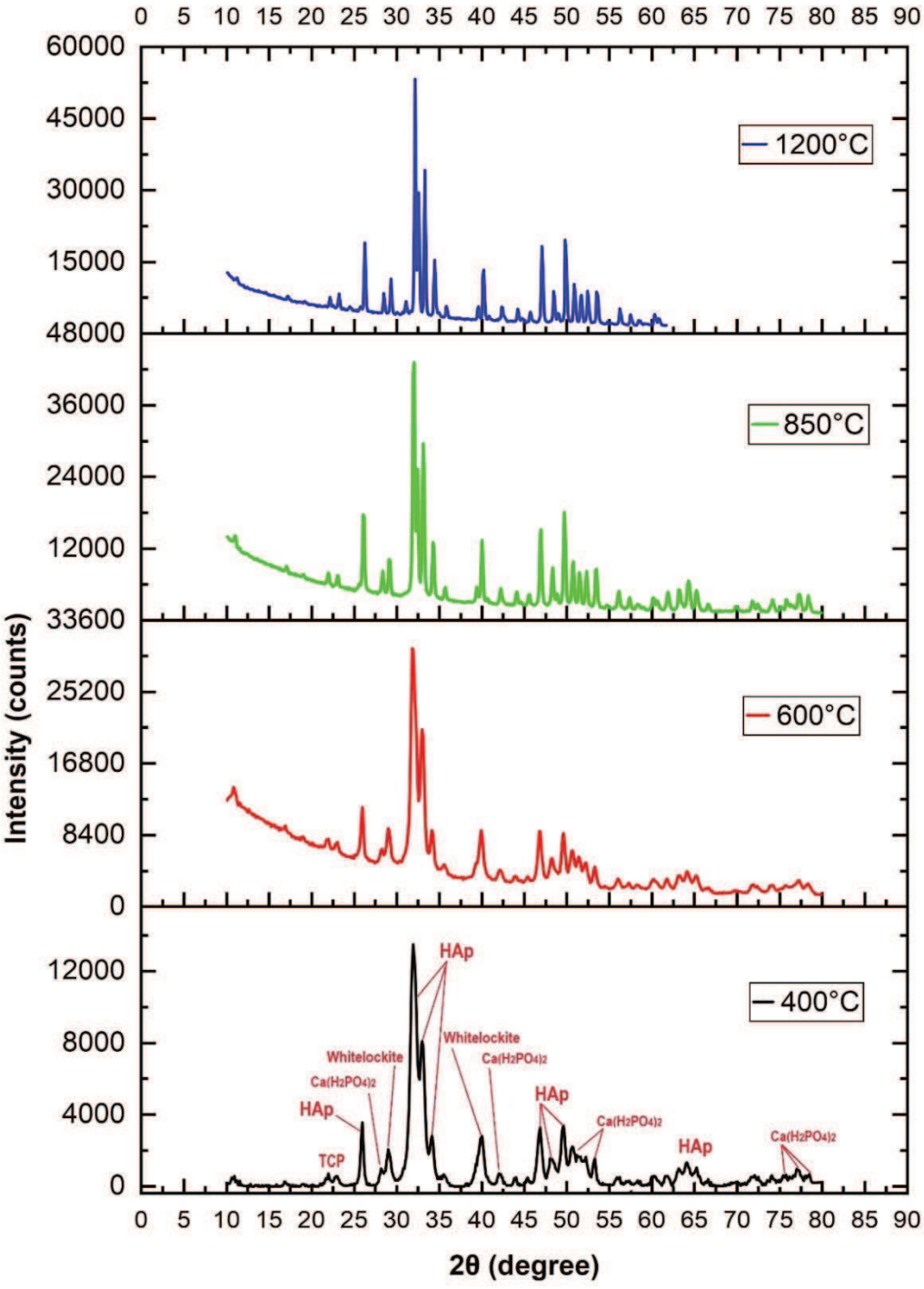

Fig.4.3. XRD Patterns for Commercial HAp Powder sintered 400-1200℃

4.2 Microstructure and FESEM microscopy

Typical images of the HAp powders are presented in fig.4.4. a-g. Different morphologies were observed among the powders. The hydrothermal and commercial HAp powders were made up of nanosized particles and consisted of soft agglomerates, whereas the sol-gel powder appeared to be composed of hard agglomerates. At the same time, the sol-gel and hydrothermal HAp powders showed a higher tendency to agglomerate.

Fig.4.4. a-d shows the SEM images of the as-dried sol-gel HAp powder obtained after heat-treatment at 750°C for 4h in stagnant air. The sol-gel powder appears to be highly agglomerated due to the many steps during formation and drying of the gel. In sol-gel synthesis, dispersing all reactants is critical and difficult, even with the use of vigorous stirring for hours. The surface-dominated properties associated with nanocrystalline particles that led these particles to cluster together, could contribute to agglomeration. The recrystallization of the dissolved calcium nitrate during gel formation and drying may result in small particles being embedded in each other and agglomerating into clusters [48]. Higher magnification indicates agglomeration of smaller sized grains in the HAp powder. The average particle size by FESEM is in the range of ~0.65μm to 1.27μm diameter length.

In the aqueous system, involving distilled water and ethanol, the hydrothermal synthesized HAp powders agglomerate in a jagged, flake-like morphology, attached to each other as shown in Fig.4.4. e. The strong electrostatic interaction between cationic surfactant CTAB Ca^{2+} and the PO_4^{3-}solution lead to HAp clusters preferentially condensed on the plate-like, rod-like surface of the micelle [49]. Fig.4.4. e shows the morphology of sintered platelets and large particle clusters, similar in many ways to the particle morphologies previously seen in the as-dried sol-gel HAp powder. The average particle size by FESEM was found to be in the range of ~5.2 μm to 7.5 μm diameter length.

For the commercial HAp sample, (Fig.4.4. f,g), it appears that very fine particles have been sintered slightly during heat-treatment based on the observed surfaces of the particles seen in the FESEM image. The sample appears to have well-defined grains of spherical particles and a uniform microstructure with different particle sizes. The average particle size by FESEM is in the range of ~2.9 µm to 17.4 µm diameter length.

Fig.4.4. a,b Microstructure of Sol-gel HAp under high resolution FESEM

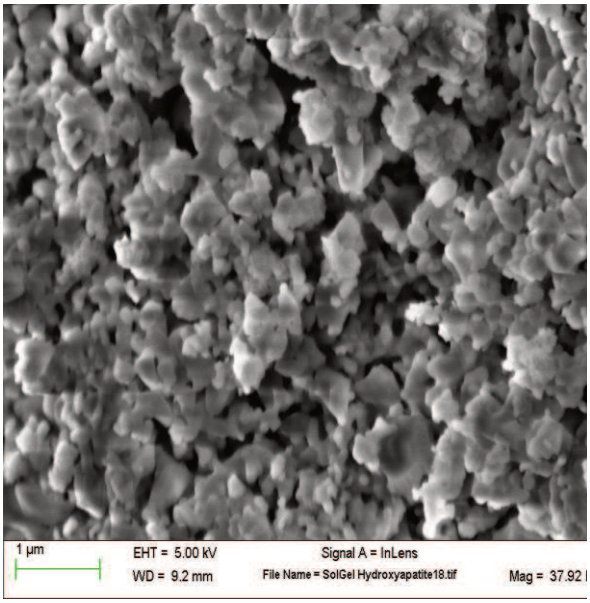

Fig 4.4. a

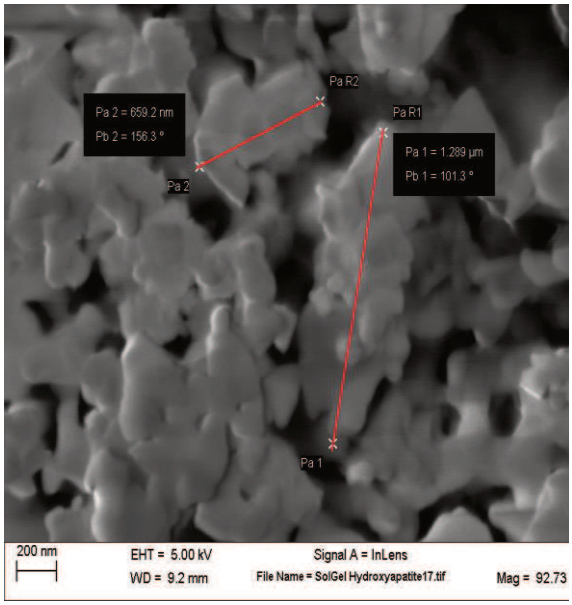

Fig 4.4. b

Fig 4.4. c

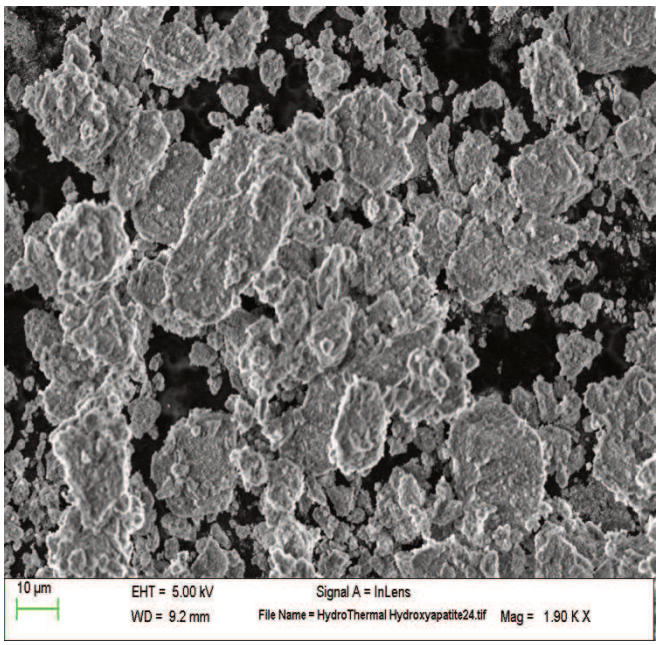

Fig 4.4. d

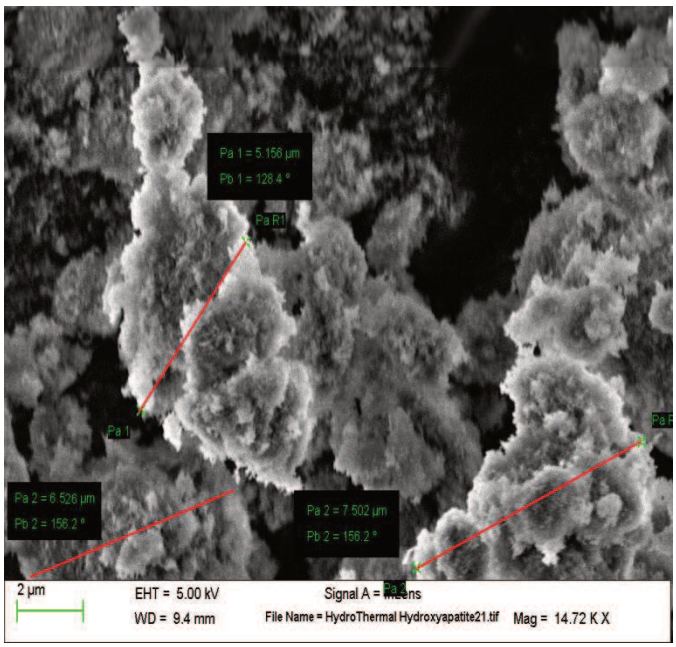

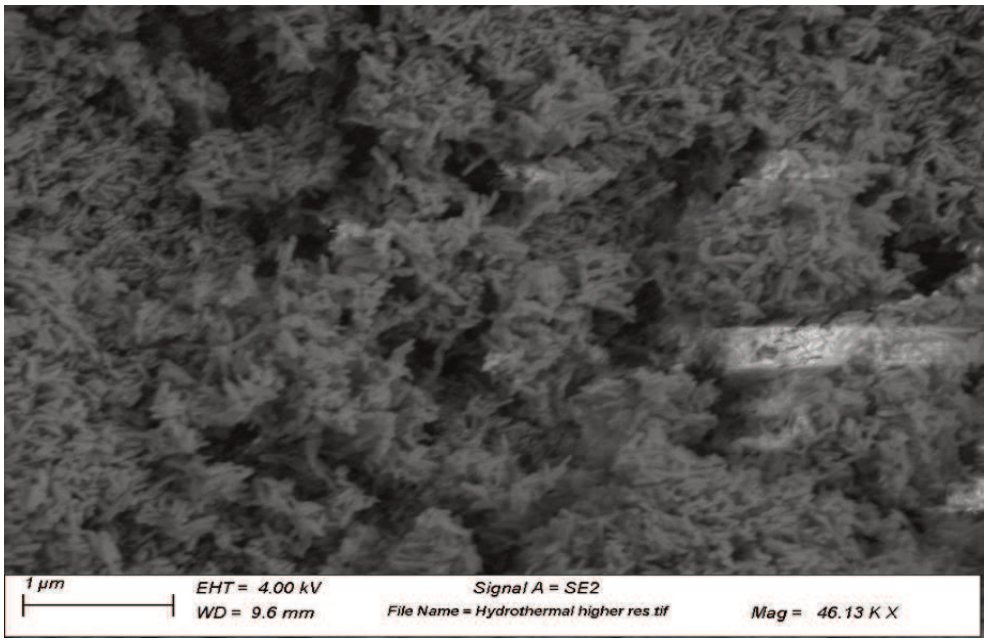

Fig.4.4. e, Microstructure of Hydrothermal HAp under high resolution FESEM

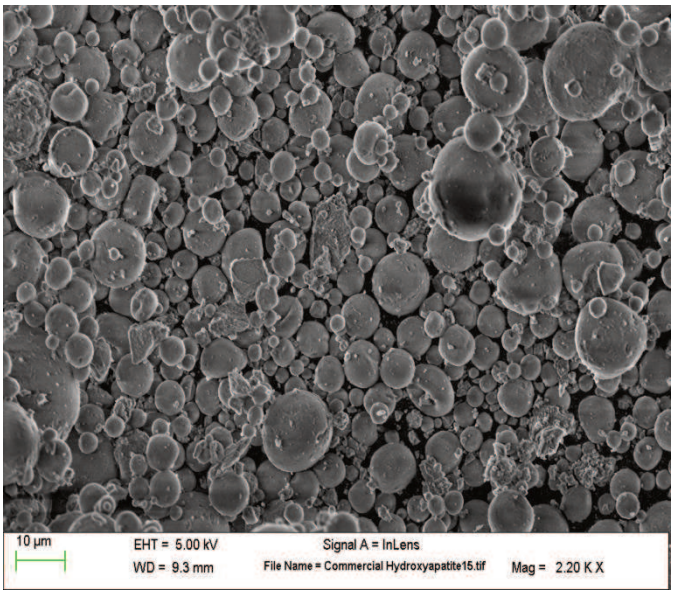

Fig.4.4. f

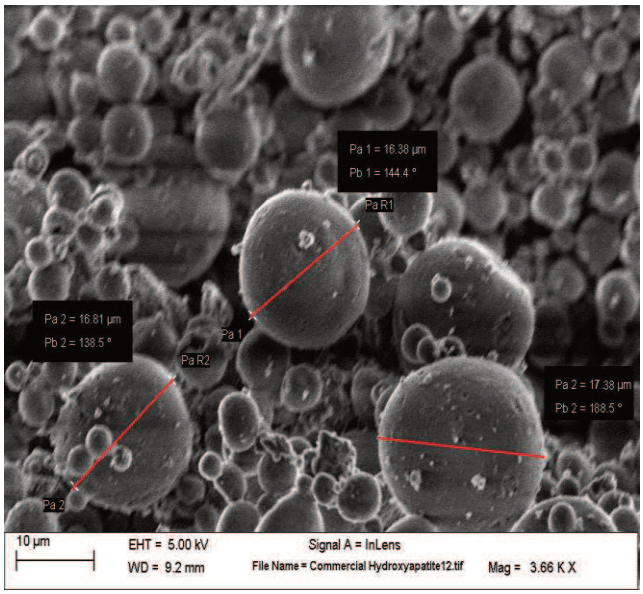

Fig.4.4. g

Fig.4.4. f,g Microstructure of Commercial HAp under high resolution FESEM

4.3 Fourier Transform Infrared Spectroscopy (FTIR)

Molecular vibrational spectroscopy is a way to identify molecular species in the powders. Depending on absorbance, transmittance or reflectance of infrared light, the most intense IR peaks in all three samples are at 565, 605, and 1032 cm^{-1}. The peaks are attributed to the PO_4^{3-} group. In addition, OH^- ions are present in HAp, and the peaks are seen at 630 and 3570 cm^{-1} in both hydrothermal and commercial HAp samples.

In the sol-gel sample (Fig. 4.5, a) the highest PO_4^{3-} peak appeared at 1046 cm^{-1} (triply degenerate asymmetric stretching mode, ν_{3b}) in addition to other phosphate group bands that were found at 963 (P-O stretching vibration peak), 875 (hydrogen phosphate group, unidentified peak, 633 and 472 cm^{-1} (double degenerate bending mode, ν_{2a}) [50]. Peaks between 1150-1270 cm^{-1} are attributable to

phosphate esters (P-O-P) as well as –OR bonds associated with alcohol groups [51]. Although the absorption peak was not significant, an OH stretching vibration band appeared at 3470 cm^{-1} [53, 54].

In the hydrothermal sample, (Fig. 4.5, b), intense PO_4^{3-} peaks appeared at 1038 and 565 cm^{-1} as ν_3 and (triply degenerate bending mode, ν_{4a}) bending vibration modes. Additional phosphate peaks were found at 1110, 975, 602 cm^{-1} (triply degenerate bending mode, ν_{4a}) and 472 cm^{-1} (double degenerate bending mode) [50]. Also, a NO_3^- band at 1383 cm^{-1} has been noticed [51]. Due to adding CTAB as a surfactant, contribution of CO_3^{2-} groups were seen in the region 1470-1440 cm^{-1} [52,54]. The absorption peak at 1631 cm^{-1} was attributed to the bending mode of H_2O [55, 56]. The hydroxyl bending band of the –OH vibration was overlapped with the sharp peak of the adsorbed water at 3585 cm^{-1}[51].

The commercial sample, (Fig. 4.5, c), showed PO_4^{3-} peaks at 1038 and 565 cm^{-1} as ν_3 and (triply degenerate bending mode, ν_{4a}) bending vibration modes. As far as this commercial sample synthesis method and precursors are unknown, the group peak at 1470 cm^{-1} might be related to either a CO_3^{2-} group or phosphate esters (P-O-P). A bending mode of H_2O is represented in the absorption peak at 1631 cm^{-1} [55]. The relative intensity at 3540 cm^{-1} is low because of calcination of the sample at higher temperatures (>800°C) for some hours. There is no evidence of P-O-P esters. However, the broad peak ranging from 3300-3600 cm^{-1} likely is due to an O-H group stretch vibration [54]. Table 4.3. shows the infrared bands assigned for the synthesized hydroxyapatites.

HAp Sample ----------	Peak position cm^{-1} ----------	Assignment ----------
Sol-gel	565, 605, 1032, 1046	PO_4^{-3} stretching mode
	963	P-O stretching vibration peak
	633, 875	hydrogen phosphate
	472	double degenerate bending mode
	1150-1270	phosphate esters (P-O-P) –OR bonds associated with alcohol groups
	3470	-OH stretching vibration band
Hydrothermal	630, 3570, 3585	-OH stretching vibration band
	565, 605, 1032, 1038, 1110, 975, 602	PO_4^{-3} bending vibration modes
	470-1440	CO_3^{-2} from CTAB
	1631	bending mode of H_2O
Commercial	630, 3570	-OH stretching vibration band
	565, 605, 1038,	PO_4^{-3}
	1470	CO_3^{-2} group or phosphate esters (P-O-P).
	1631	bending mode of H_2O
	3300-3600	-OH stretching vibration band

Table 4.3. Infrared bands assigned for the synthesized hydroxyapatites

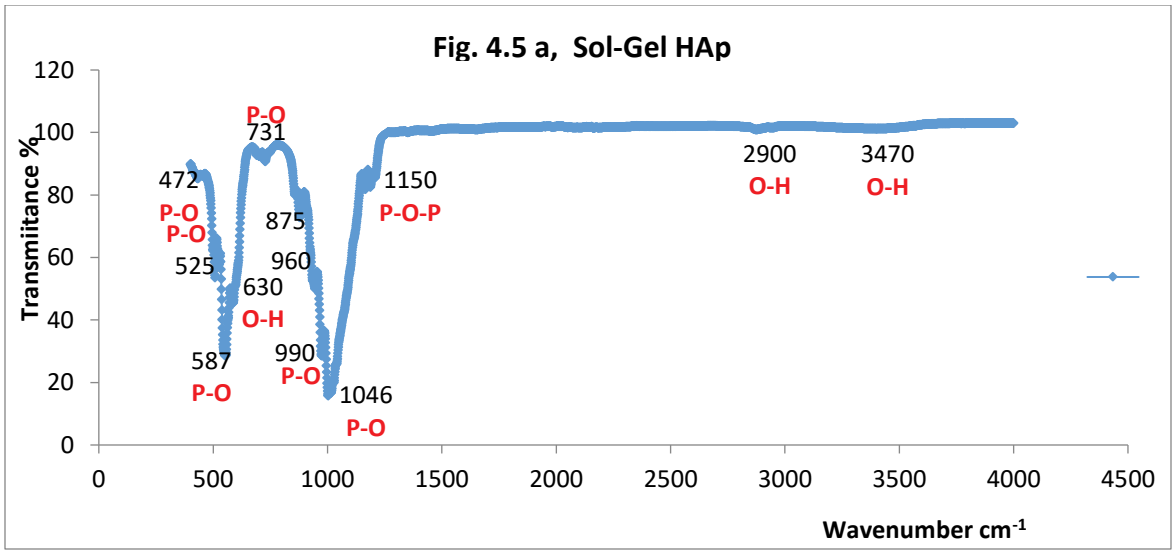
Fig. 4.5 a, Sol-Gel HAp
Transmiitance %
120
100
80
60
40
20
0
0
500
1000
1500
2000
2500
3000
3500
4000
4500
Wavenumber cm-1
P-O
731
472
P-O
P-O
875
525
960
630
O-H
587
P-O
990
P-O
1046
P-O
1150
P-O-P
2900
O-H
3470
O-H

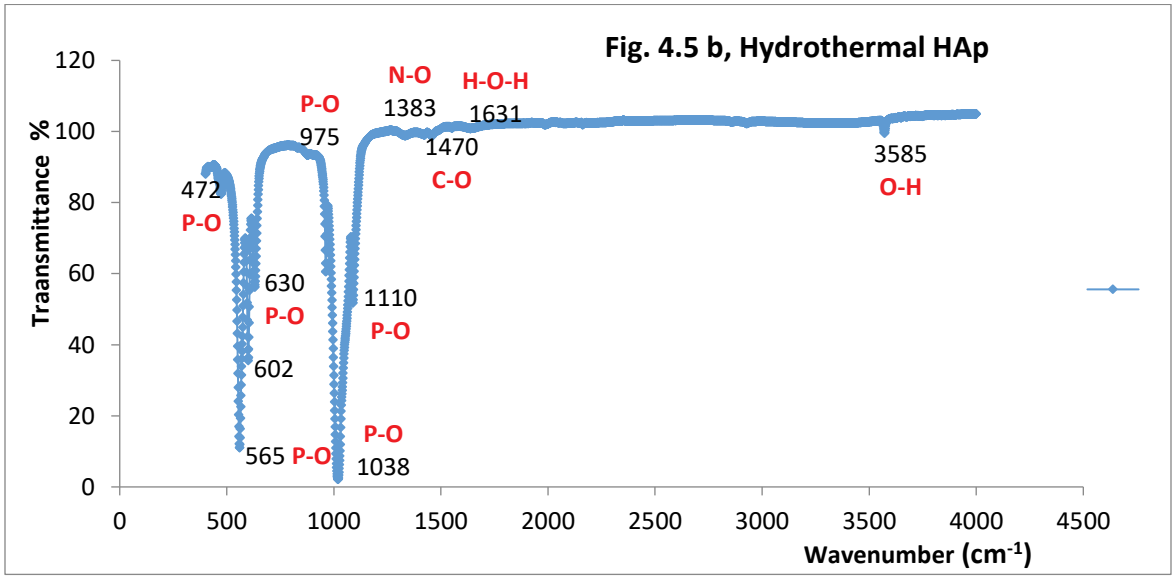
Fig. 4.5 b, Hydrothermal HAp
Traansmittance %
120
100
80
60
40
20
0
0
500
1000
1500
2000
2500
3000
3500
4000
4500
Wavenumber (cm-1)
N-O
H-O-H
P-O
1383
1631
975
1470
C-O
3585
O-H
472
P-O
630
P-O
1110
P-O
602
P-O
565 P-O
1038

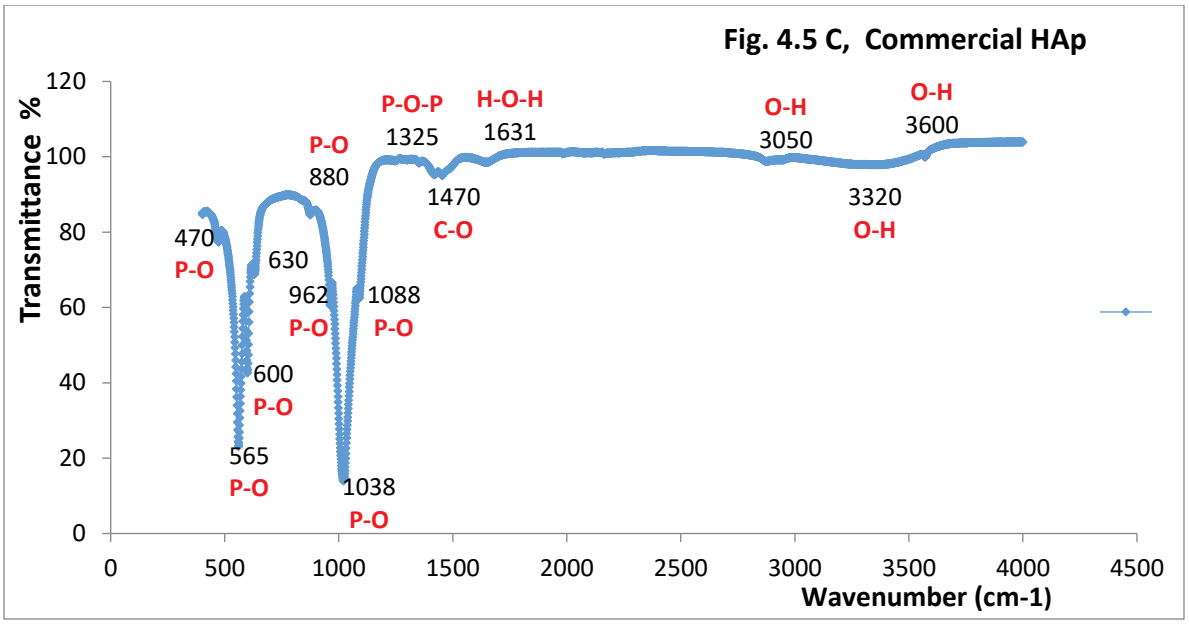

Fig. 4.5, a-c FTIR graphs for as synthesized HAp powders.

4.4 Thermogravimetric (TGA) Analysis and Differential Scanning Calorimetry (DSC)

Thermal analysis is the main method for predicting the changes (glass transition temperature, energy liberated, reaction types exothermic or endothermic and weight loss) or thermal stability taking place in the as prepared HAp powders when subjected to heat treatment. Thermal analysis in terms of TGA and DSC were carried out for the prepared powders in both air and nitrogen N_2. Samples weights and heat flows were recorded.

4.4.1 TGA and DSC in Nitrogen gas

The thermal analysis plots for the three samples (sol-gel, hydrothermal, and commercial powders) in nitrogen are shown in Figure 4.6. a-d. Thermogravimetric analysis (TGA) was conducted on the as-synthesized powders in N_2 with a heating rate 20°C per minute from room temperature up to 1200°C. This method was used to determine the phase stability and reaction temperatures of the HAp powders.

The as-synthesized sol-gel sample (fig.4.6, a) shows about 5.5% total weight loss up to 1200°C with a constant stable weight above 800°C. The first weight loss accompanied by an endothermic peak is observed at 200°C and is associated with the evaporation of adsorbed water, followed by removal of structural water in the precursor $Ca(NO_3)_2 \cdot 4H_2O$. At that temperature, the sample showed 4% weight loss. This removal of water was also observed in the DSC curve, with an endothermic peak and a small shift in the baseline. The second weight loss in the range ~255-400°C corresponds to the removal of $–NO_3$ groups, associated with the alkoxy-nitrate species in the precursors along with the removal of –OH [57]. The second exothermic peak in the DSC scan supports the removal of these species in this temperature range. In addition, there is a slight weight loss of 0.5% in the range of ~420-800°C in the sol-gel sample, which corresponds to crystallization of HAp above 400°C [57]. The crystallization peak in the DSC curve begins at ~310°C.

In the TGA plot for the hydrothermal powder, (fig.4.6, b), the total weight loss was ~4%, as compared to 5.5% for the sol-gel sample. Adsorbed water evaporated at ~ 280°C and the weight loss of evaporation at that point was 2%. The DTA curve shows an endotherm at 850°C assigned to the decomposition of entrapped nitrate groups in the lamellar structure of HAp, which is supported by the FTIR results of having an NO_3^- band at 1383 cm^{-1} [51]. Exothermic peaks below the decomposition temperature indicate crystallization. Crystallization to HAp occurs around 900°C, which is higher than the crystallization temperature in the sol-gel powder.

The commercial HAp, (fig.4.6, c), showed the largest weight loss, over 13.5% of the original starting weight. This weight loss is due to the commercial powder having more water adsorbed on the particles surfaces than the sol-gel or hydrothermal powders. This powder had the highest specific surface area according to nitrogen sorption measurements. HAp is a hygroscopic material, and hence the primary component adsorbed on the surface is water [59]. Adsorbed water evaporates from the

particles between ~110 and 200°C causing a 3.6% weight loss and the first endothermic peak. The TGA curve above 900°C shows a steady weight loss. However, the DSC curve shows an exothermic peak indicating crystallization.

For all three HAp samples, dehydration did not completely happen even after firing up to 1200°C as seen in the O-H bands found in FT-IR spectra of the calcined samples. All DSC curves show smaller endothermic peaks in the range of 650-750°C, which indicate the expenditure of heat for a phase change. XRD results showed two crystal HAp phases for each sample.

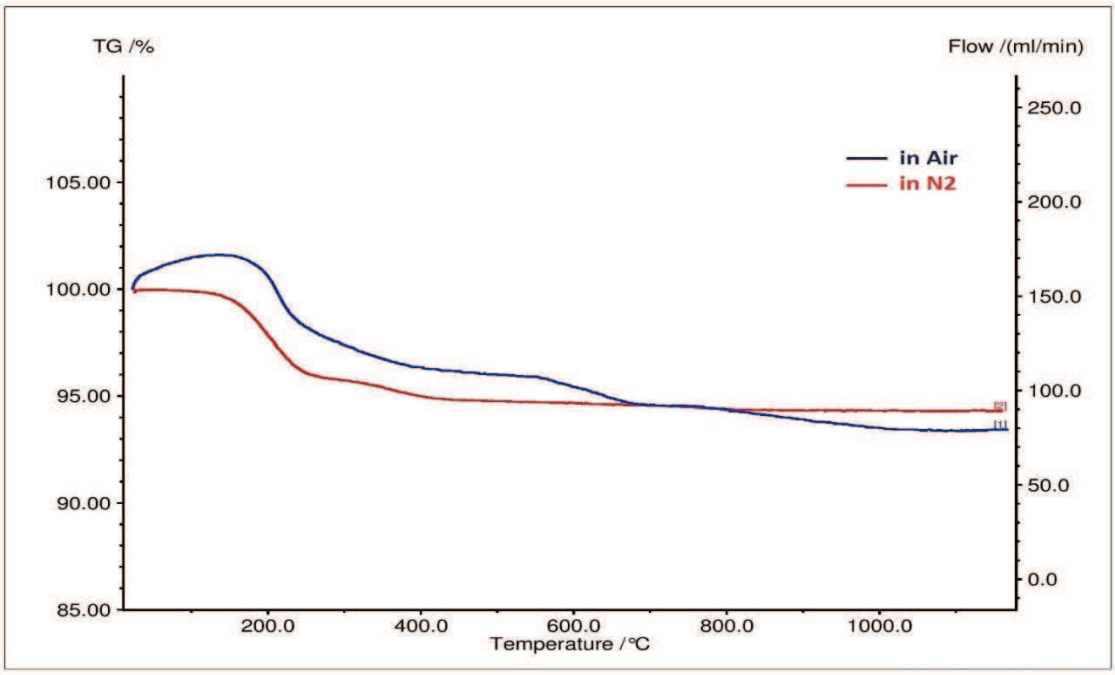

Fig.4.6. a, TGA of sol-gel HAp in Air and N_2

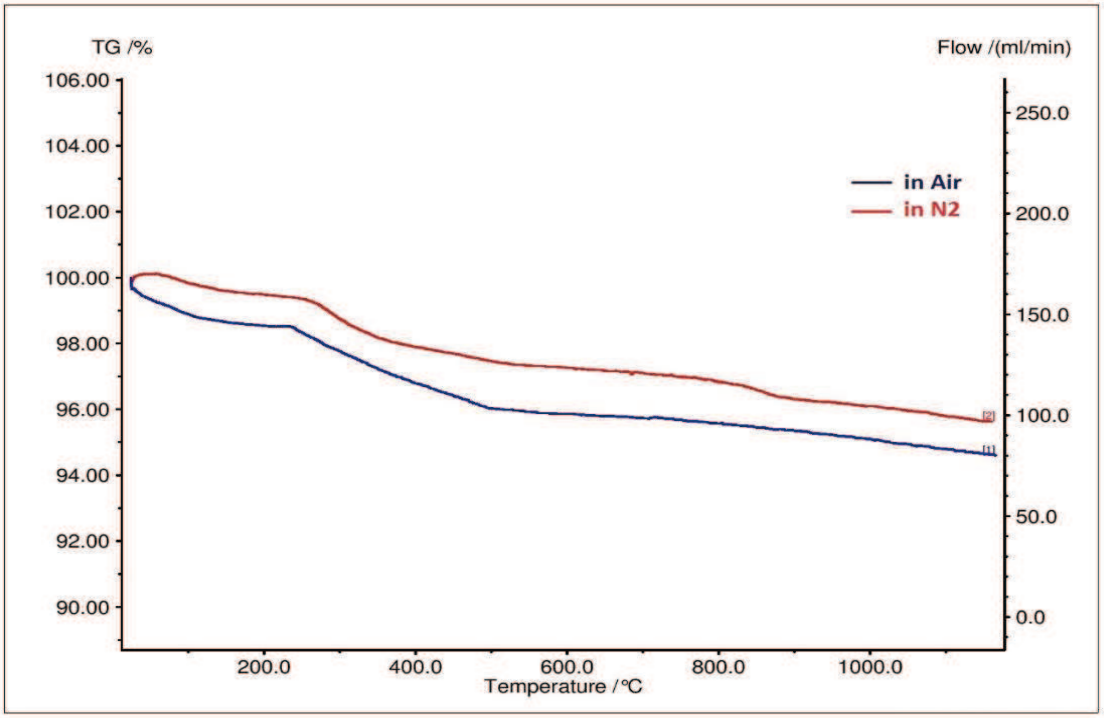

Fig.4.6. b, TGA of hydrothermal HAp in Air and N_2

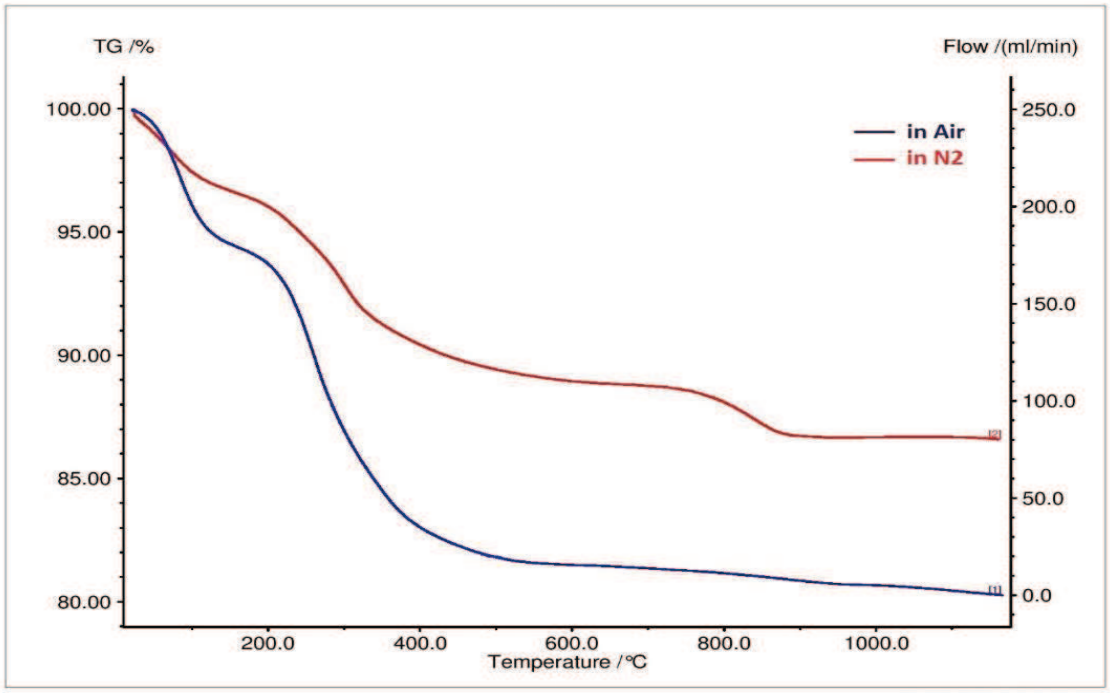

Fig.4.6.c, TGA of commercial HAp in Air and N_2

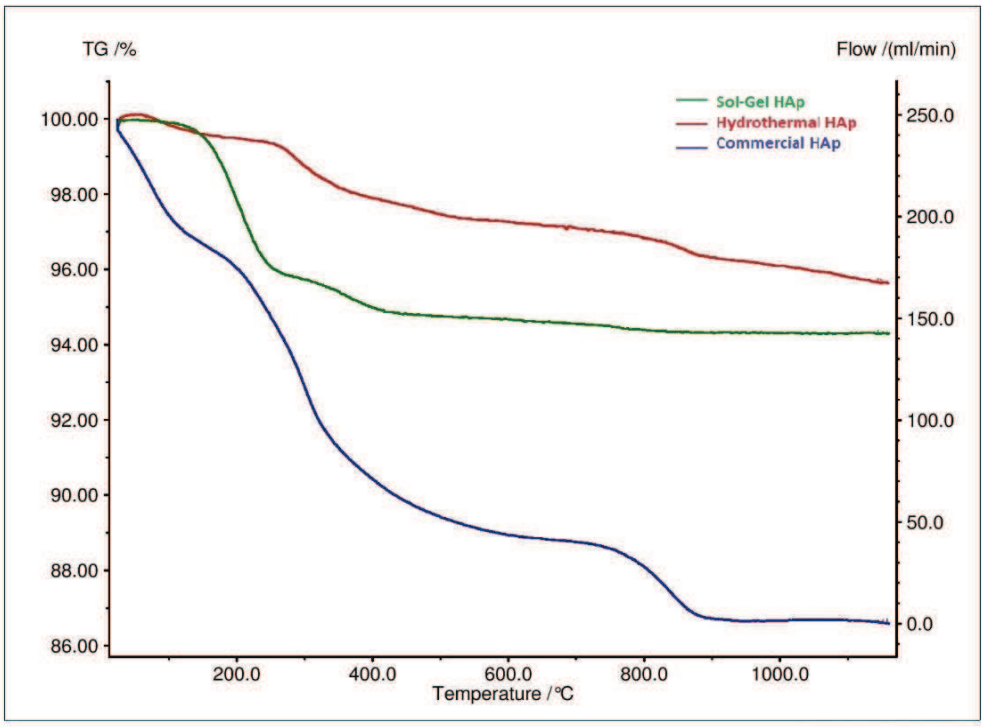

Fig.4.6. d, Comparison of TGA graphs of sol-gel, hydrothermal, and commercial HAp in N_2

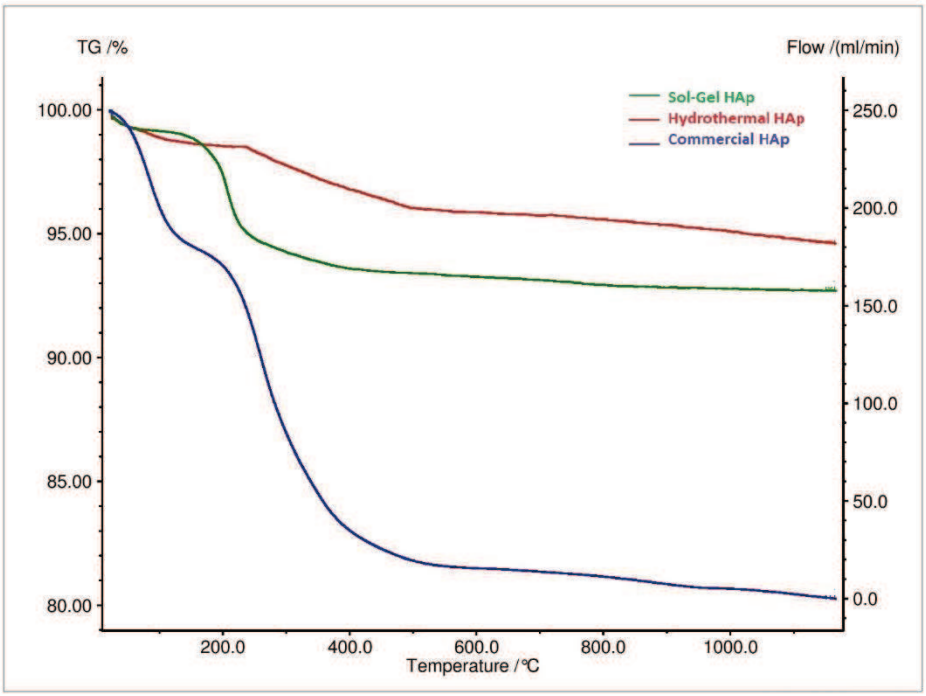

Fig.4.6. e, Comparison of TGA graphs of sol-gel, hydrothermal, and commercial HAp in Air

4.4.2 TGA and DSC in Air

Results of running TGA and DSC analysis for the sol-gel, hydrothermal, and commercial samples in air are shown in fig.4.7. a-c. Thermogravimetric analysis (TG) was conducted on the three HAp powders in air with 20°C per minute heating rate from room temperature up to 1200°C.

The as-synthesized sol-gel sample, (fig.4.7, a), shows about 6.6% total weight loss up to 1200°C with a constant weight loss after 1100°C. The first weight loss of an endothermic peak is observed at ~180°C associated with the evaporation of adsorbed water, followed by removal of structural water in the precursor $Ca(NO_3)_2 \cdot 4H_2O$. At that temperature, the sample showed 1.5% weight loss. This removal of water was also observed in the DSC curve, with an endothermic peak. The second weight loss in the range 200-400°C corresponds to the removal of $-NO_3$ groups, associated with the alkoxy-nitrate species in the precursors along with the removal of OH^- [57]. The second exothermic peak in the DSC scan supports the removal of these species in this temperature range. In addition, there is a slight weight loss of 0.7% in the range of 400-1200°C in the sol-gel sample, which corresponds to crystallization of HAp above 400°C [57]. The crystallization peak in the DSC curve begins at ~250°C.

In the TGA plot for the hydrothermal powder, (fig.4.7, b), the total weight loss was 5.7% as sintering temperatures reached 1200°C with a constant weight loss after 750°C. Adsorbed water evaporated above 250°C as the first endotherm was detected at that temperature. The sample lost nearly 2% of weight by water evaporation. Exothermic peaks below the decomposition temperature indicate crystallization. Crystallization in the hydrothermal HAp sample started around 550-600°C, which is lower than the crystallization temperature in the sol-gel powder.

Same as in nitrogen, the commercial HAp, (fig.4.7, c), showed the largest weight loss, over 19.5% of the original starting weight. This weight loss is due to the commercial powder having more water adsorbed to the particles surfaces than the sol-gel or hydrothermal powders. Recall that this

powder had the highest specific surface area according to nitrogen sorption measurements and is hygroscopic [59]. Adsorbed water started to evaporate from the sample at ~95°C causing a 4% weight loss and the first endothermic peak. The TGA curve above 950°C shows a steady small weight loss. However, the DSC curve shows an exothermic peak indicating crystallization. The DSC curve shows a broad endothermic peak in the range of 400-550°C, which indicates the expenditure of heat for a phase change of HAp confirmed by the XRD results of the sintered powder.

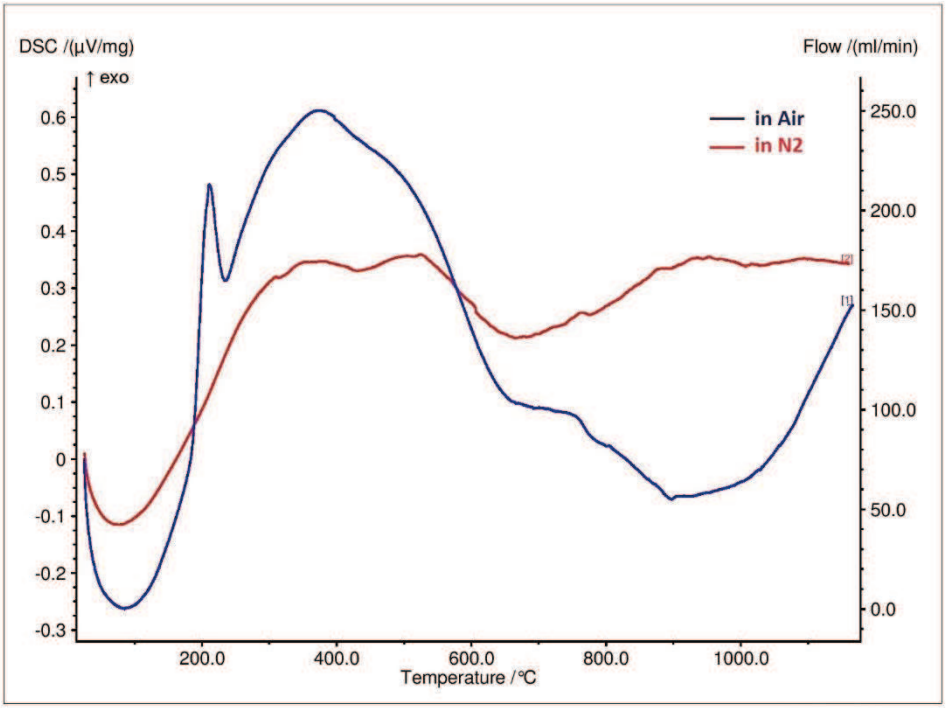

Fig.4.7, a, DSC of Sol-Gel HAp in Air and N_2

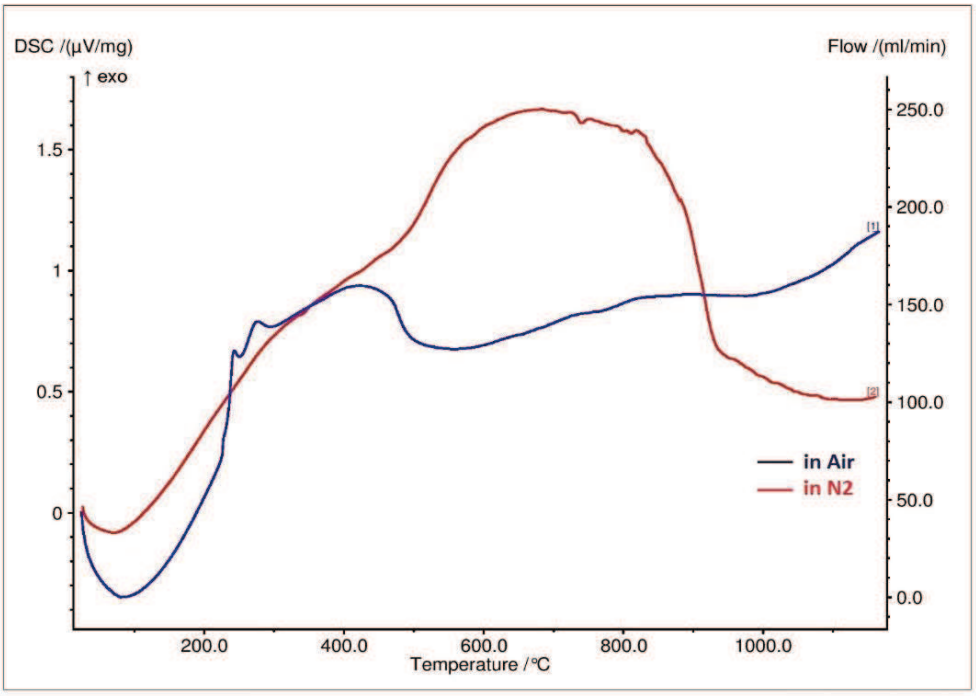

Fig.4.7, b, DSC of Hydrothermal HAp in Air and N_2

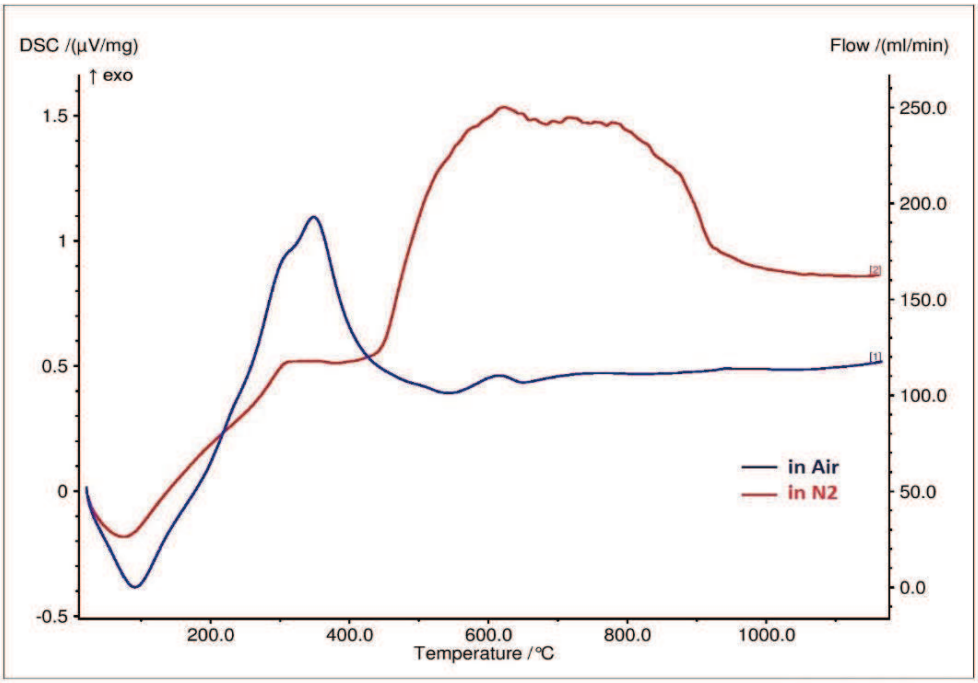

Fig.4.7, c, DSC of Commercial HAp in Air and N2

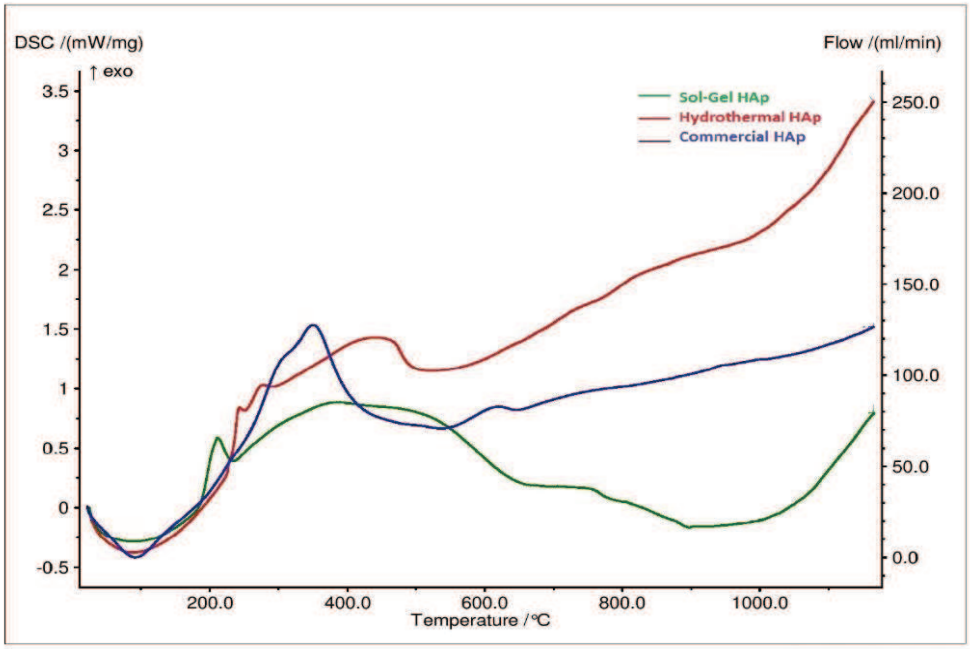

Fig.4.7, d, Comparison of DSC graphs of Sol-Gel, Hydrothermal, and Commercial HAp in Air.

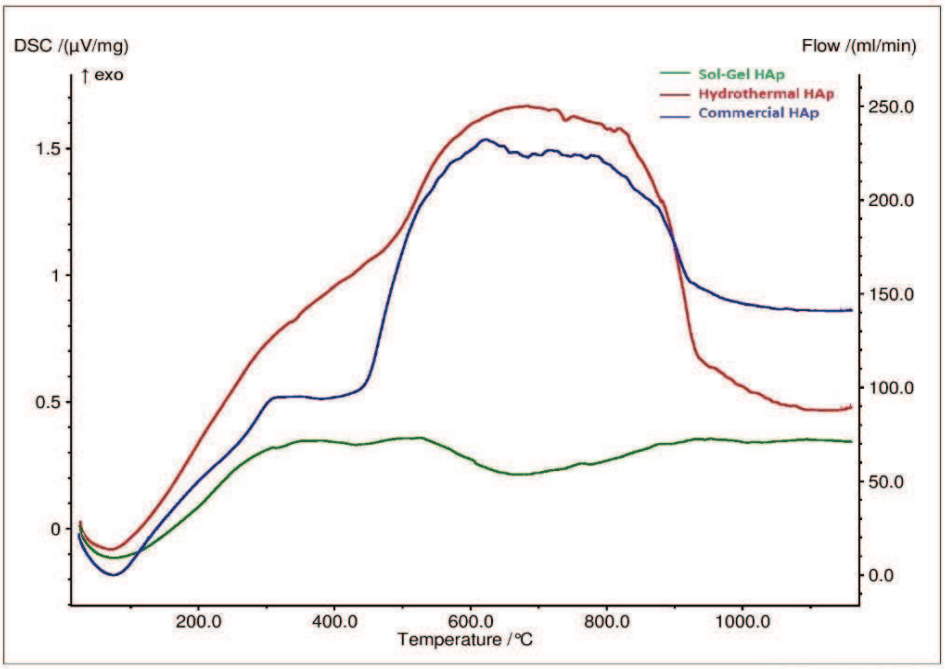

Fig.4.7, e, Comparison of DSC graphs of Sol-Gel, Hydrothermal, and Commercial HAp in N_2

Table 4.4.1. Sol-gel HAp TGA and DSC graph

Assignment	In Air	In Nitrogen
Total weight loss	6.6%	5.5%
Adsorbed water evaporation	180℃ (4% w.loss)	200℃ (first endothermic peak) (1.5% w.loss)
Crystallization temp.	250℃ (DSC)	310-400℃
Constant weight loss	200-400℃	255-400℃ ($–NO_3$, -OH) removal, (second exothermic peak)

Table 4.4.2. Hydrothermal TGA and DSC graph

Assignment	In Air	In Nitrogen
Total weight loss	5.7%	4%
Adsorbed water evaporation	200℃ (2% w.loss)	280℃ (first endothermic peak) (2% w.loss)
Crystallization temp.	600℃	900℃ (exothermic)
Constant weight loss	750℃	1000℃ ($–NO_3$, -OH) removal, (second exothermic peak)

Table 4.4.3. Commercial TGA and DSC graph

Assignment	In Air	In Nitrogen
Total weight loss	19.5%	13.5%
Adsorbed water evaporation	95-110℃ (4% w.loss)	110-200℃ (first endothermic peak) (3.7% w.loss)
Crystallization temp.	350℃	900℃ (exothermic)
Constant weight loss	950-1000℃	880℃, (second exothermic peak)

4.5 Brunauer-Emmett-Teller (BET) Surface Area

The Brunauer-Emmett-Teller (BET) surface area measurements of the HAp powders were carried out using nitrogen gas to obtain the surface area measurement. The results are presented in table 4.2, using the ISO 9277 standard for calculating the specific surface area of solids [61].

Property	Sol-Gel HAp	Hydrothermal HAp	Commercial HAp
BET Surface Area m^2/g	6.126 ± 0.065	35.928 ± 0.402	52.386 ± 0.151
BET at P/Po = 0.291 m^2/g	5.847	34.538	49.566
Adsorption cumulative volume of pores cm^3/g	0.0768	0.4467	0.217
Particle size range (µm)	0.58- 30.59	2.09 - 61.68	2.49 - 161.39
Dominating particle size (µm)	24.10	35.335	35.335

Table 4.5: BET Surface area, Particle size distribution, Crystallite sizes and indices of the as-synthesized HAp powders.

4.6 Average Particle Size Distribution

The average particle size and particle size distribution for each powder is listed in table 4.2. Figure 4.8, a-c shows the average particle size distributions.

The order of mean particle size from largest to smallest is as follows: Commercial HAp > Hydrothermal HAp > Sol-Gel HAp. The particle size distribution of the sol-gel HAp possesses a bimodal distribution. The bimodal graph is due to the slow dripping rate of the calcium precursor into the phosphate solution, which caused gradual gelation and possible aggregation of HAp. However, most of the Sol-Gel HAp particles are in 11.2 – 42.6 µm range. An increase in the reaction temperature can significantly increase the resulting particle size in a Sol-Gel HAp preparation, while stirring speed for the same method had shown some effect on tailoring the desired particle size [40].

The wide range of distribution in the Commercial powder sample, 0.41-586. µm crosses the 100 µm limit which is required in a powder for successful nozzle injection [121]. Therefore, this powder will need further steps of separation/sieving to be useful in 3D printing. Most of the hydrothermal HAp particles are in 18.7 – 66.9 µm range, with a small fraction of particles showing a maximum size of 98.1 µm, which is suitable for better 3D printing procedure.

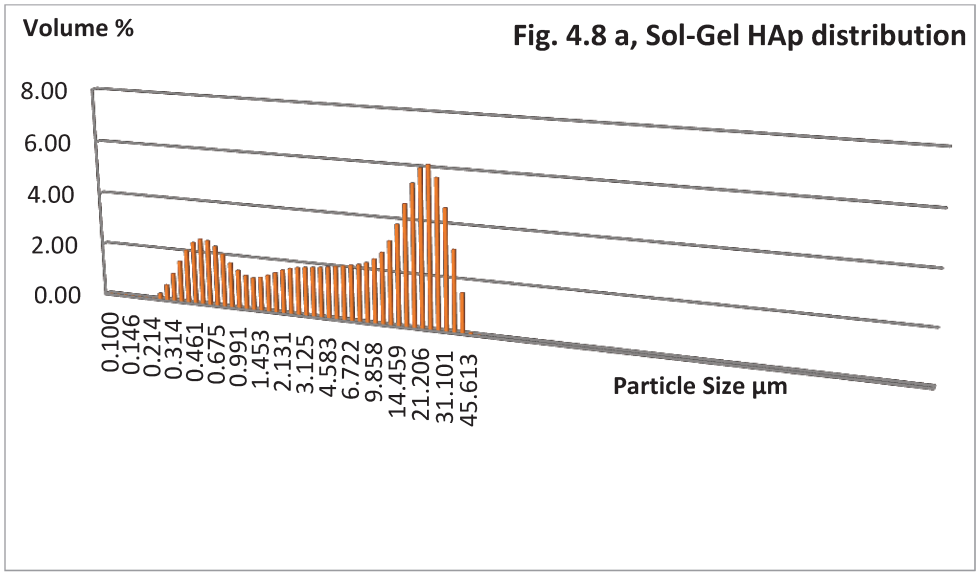

Fig. 4.8 a, Sol-Gel HAp distribution

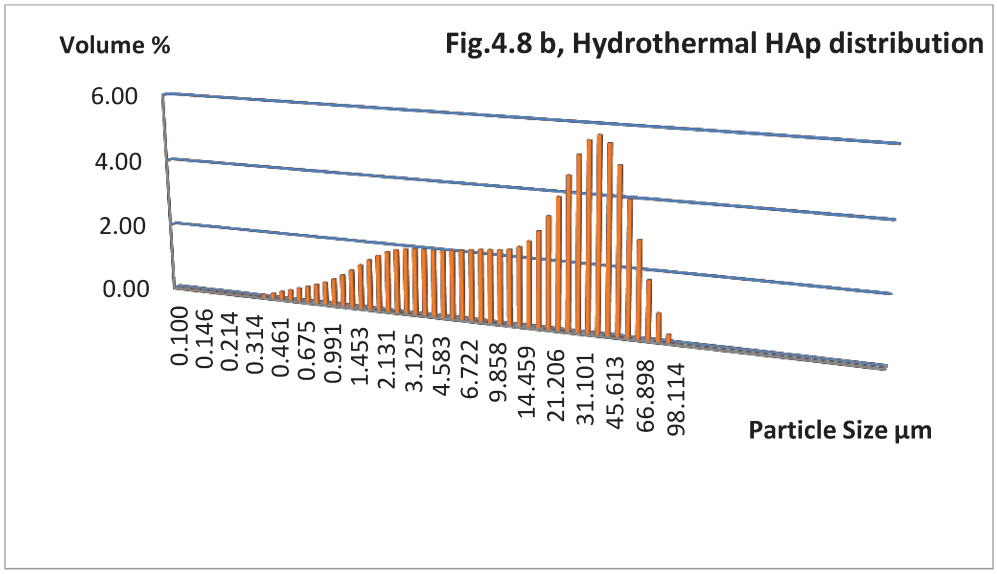

Fig.4.8 b, Hydrothermal HAp distribution

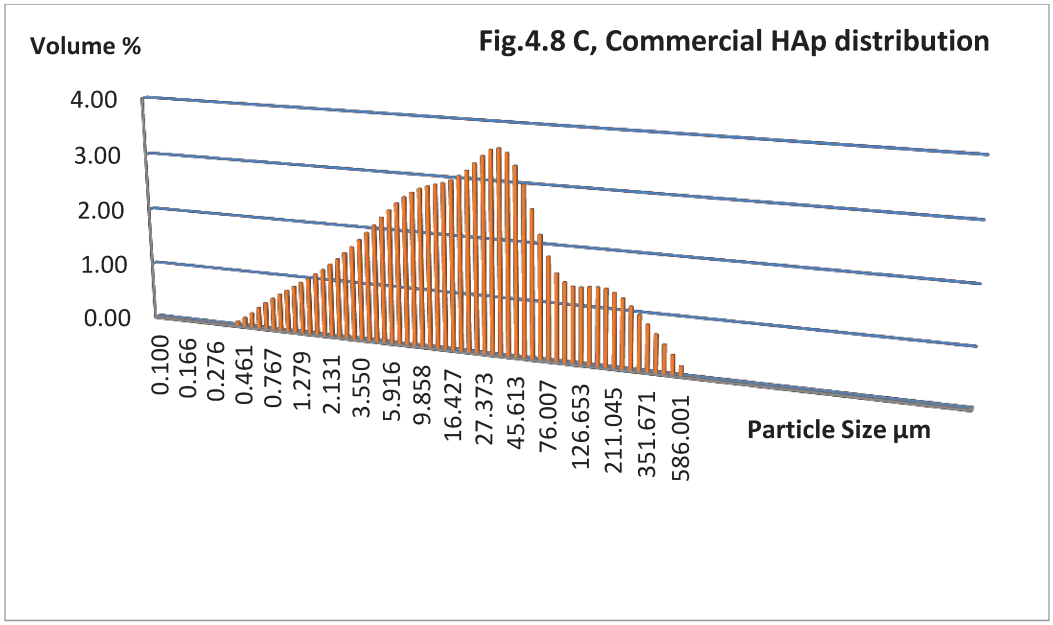

Figure 4.8, a-c Average particle size distributions of the hydroxyapatite powders

Chapter Five

Conclusions and Suggestions for Future Work

5.1 Conclusion

This dissertation is a comparison study of three different hydroxyapatite powders synthesized through three different methods: sol-gel, hydrothermal, and a commercial sample. The aim is to determine which of these methods produces HAp that achieves most requirements for a desirable 3D printed biomaterial scaffold for in vivo applications. The study focused on the differences of preparation methodology on the microstructural properties, phase composition, particle size and crystallinity.

The sol-gel method provided a homogeneous molecular mixing at a low processing temperature (<95°C). The resulting apatite structure mainly depended on the chemical nature of the precursors in terms of chemical activity and the heat treatment temperature. Such apatite has crystal sizes in the range of enamel [42]. It is recommended in a sol-gel synthesis to have a longer aging period of the gel before drying in addition to specific sintering protocols to avoid cracking in 3D structures [35].

The hydrothermal technique produced crystalline HAp in one step without requiring post heat treatment by crystallizing HAp directly from the aqueous solution. However, the scalability of this technique is limited to the size of the reaction vessel [51]. XRD analysis and FESEM characterization showed that hydrothermal powder had a single phase of needle-like HAp particles similar to what was found in the literature review [52]. These HAp particles could be tailored through the control of the process temperature, the reaction time, concentration of CTAB, and the pH value of the solution [57].

The single phase purity and more uniform crystallites were shown by XRD after exposure to higher sintering temperatures. These characteristics of the hydrothermal HAp resulted in better thermal stability. This makes it a good bioceramic powder for further incorporation into polymer composites for biomedical applications.

As particle shape and size affect the densification, sinterability, as well as solubility of HAp for implant applications, the three powders were examined for BET and particle size. With a small difference in values, both hydrothermal and commercial HAp had a higher BET than the sol-gel powder. Higher surface area and surface roughness result in better cell adhesion and bone regeneration [7, 114]. Researchers related stronger 3D printed HAp parts to large pre-coated particles because of the better densification of intra-particles than inter-particles during the sintering process [89]. Hydrothermal HAp, similar to the commercial HAp, appears to follow this trend with a larger dominating particle size.

The adsorption isotherm showed a larger pore volume in the hydrothermal sample, while sol-gel powder showed less pore volume due to agglomeration. Micro-porosity is vital for fluid exchange and cellular influx during bone healing. The size and shape of pores of granular HAp used in 3D printing can affect vascularization, cell migration, and angiogenesis in vivo [86] because it is essential for any successful transplantation to have interaction with endogamous tissues.

Following the 3D printing process, heat treatment and firing are required to manage binder content and stabilize pores in the structure. Sintering of HAp is difficult due to the presence of the OH content, and poor sinterability does not degrade the hardness of HAp [58]. Regarding that, weight losses in DSC-TGA plots of the three HAp powders were studied and indicated major differences when the powders were heated in air vs nitrogen. All HAp samples,

regardless of synthesis method, experienced higher total weight losses in air than nitrogen. Sintering and heat treatment in air made the evaporation of crystalline and adsorbed water in the precursor faster at lower temperatures. This was observed in the first endotherm peak in each graph. The second weight loss endotherm in the graphs was attributed to the removal and decomposition of entrapped nitrate substances. In air, all samples showed an endotherm at lower temperatures (~ 600°C) as compared to heating in nitrogen. The third weight loss corresponds to the high temperature exotherm which indicates the crystallization of the HAp phase. Crystallization in air occurred at lower temperatures compared to nitrogen.

In conclusion, hydrothermal HAp powder has most of the preferred qualifications for 3D printing and bio applications, as compared to sol-gel and commercial HAp samples. Hydrothermal HAp showed high crystallinity at different elevated sintering temperatures. The active surface area, the needlelike morphology, and higher pore volume are important considerations in a scaffold, where they promote higher cell adhesion and growth. In addition, hydrothermal HAp has reasonable crystal sizes in the range of human bone and enamel

5.2 Suggestions for Future work

1- Further studies under different atmospheres, thermal conditions, and chemical solutions, and more compression to other HAp synthesize methods will be needed to fully understand the properties of the material and the behavior when applied in 3D printing.
2- Studying the influence of higher calcium excess in HAp to see the limitations that could affect nozzle injection when the ink becomes very sticky due to the inter-particles attractive force that hardens the cement.

3- Thermal studies such as dilatometric studies (TMA) to reveal the shrinkage behavior of HAp bulks regarding different synthesis routes.

4- Optimizing pore size becomes essential for molecular signaling, nutrition supply, waste removal, vascularization, and tissue studies in vitro and in vivo. In that case, further research should be done on sol-gel HAp to result into higher properties that meets 3D bio applications.

5- Evaluating the ease of incorporation into different bio compatible 3D inks and based on the rheology of the paste and the characteristics of the powder, studying the viscosity of the ink in terms of shear dependence and temperature dependence.

6- Further research on 3D scaffolds made of two or more different HAp powders from different synthesis routes. Such study will show which HAp will dominate and be responsible for higher mechanical strength or bioactivity.

References

1. Larry Hench, “Bioceramics”, Journal of American Ceramic Society, Vol. 81, Issue7, (1998), pp.1705–1728.
2. S. Abd Aljabbar, S.S. Rahmatallah,A. Al- Sarraf, Z.Shehap and H. I.Dumbous “Preparation of Fine Hydroxyapatite (HA) Powder and Its Characterization as Ceramic Biomaterial”, Ibn Al-Haitham Journal for Pure and Applied Science, No. 3 Vol. 25, (2012), pp. 127-132.
3. Guoping Chen, Takashi Ushida, Tetsuya Tateishi, “Scaffold Design for Tissue Engineering”, Macromolecular. Bioscience, No. 2, Vol. 2, (2002), pp. 67-77.
4. Masahiro Okada, and Tsutomu Furuzono, “Hydroxyapatite nanoparticles: Fabrication methods and Medical applications”, Sci. Technol. Adv. Mater. 13, (2012), pp. 14.
5. M.P. Ferraz, F.J. Monteiro, C.M. Manuel, “Review on HA nanoparticles: Preparation Methodologies”, Applied Biomaterials & Biomechanics, (2004), pp. 74-80.
6. E. Bouyer, F. Gitzhofer, M. Boulos, "Morphological study of hydroxyapatite nanocrystal suspension", Journal of Materials Science: Materials in Medicine, Vol. 11, No.8, (2000), pp. 523–531.
7. Mehdi Sadat-Shojai, Mohammad-Taghi Khorasani, Ehsan Dinpanah-Khoshdargi, Ahmad Jamshidi, “Synthesis methods for nanosized hydroxyapatite with diverse structures”, Journal of Acta Biomaterialia, Vol.9, (2013), pp. 7591–7621

8. JC Elliott, RM Wilson and SEP Dowker, “APATITE STRUCTURES”, International Centre for Diffraction Data, Advances in X-ray Analysis, Vol.45, (2002), pp. 172-181.
9. Yasushi Suetsugu, Tetsuya Tateishi, “Implants and biomaterials (Hydroxyapatite)”, Biomed Mater Res B, Vol. 85B, (2008), pp. 279-299
10. Sophie C. Cox, John A. Thornby, Gregory J. Gibbons, Mark A.Williams, Kajal K. Mallick, “3D printing of porous hydroxyapatite scaffolds intended for use in bone tissue engineering”, Materials Science and Engineering, C 47, (2015), pp. 237–247
11. Susmita Bose,w Ashis Banerjee, Sudip Dasgupta, and Amit Bandyopadhyay, “ Synthesis, Processing, Mechanical, and Biological Property Characterization of Hydroxyapatite Whisker-Reinforced Hydroxyapatite Composites”, J. Am. Ceram. Soc., Vol. 92, No.2, (2009), pp.323–330.
12. Frank Wittea, Frank Feyerabendb, Petra Maierb, Jens Fischera, Michael Stormer, Carsten Blawertb, Wolfgang Dietzelb, and Norbert Hort, “Biodegradable magnesium–hydroxyapatite metal matrix composites”, Biomaterials, Vol.28, (2007), pp. 2163–2174
13. Francois Barthelatn, and Reza Rabiei, “Toughness amplification in natural composites”, Journal of the Mechanics and Physics of Solids, Vol. 59, (2011), pp.892-840.
14. Dhivyaa Anandan, Amit Kumar Jaiswal, “Synthesis and characterization of human bone-like hydroxyapatite using Schiff's base”, Ceramics International, Vol.44, (2018), pp. 9401–9407.

15. G. Bezzi, G. Celotti, E. Landi, T.M.G. La Torretta, I. Sopyan, A. Tampieri, “A novel sol-gel technique for hydroxyapatite preparation”, Materials Chemistry and Physics, Vol.78, no.3, (2003), pp.816–824.
16. A. Chaudhry, S. Haque, S. Kellici, P. Boldrin, I. Rehman, F. a Khalid, J. a Darr, “Instant nano-hydroxyapatite: a continuous and rapid hydrothermal synthesis”, Chemical Communications, issue.21, (2006), pp.2286–2288.
17. H.S. Gupta, F. Guitia, “An Effective Morphology Control of Hydroxyapatite Crystals Via Hydrothermal Synthesis”, Crystal Growth & Design, Vol.9, No.1, (2009), pp.466–474.
18. T. Fatma, S. Balci, “Synthesis and characterization of hydroxyapatite”, Gazi University Journal of Science, Vol.21, (2007), pp.21–31.
19. D. Mehta, S. George, P. Mondal, “Synthesis of hydroxyapatite by chemical precipitation, technique and study of its biodegradability”, International Journal of Research in Advent Technology, Vol.2, (2014), pp.159–161.
20. S. Pramanik, A.K. Agarwal, K.N. Rai, A. Garg, “Development of high strength hydroxyapatite by solid-state-sintering process”, Ceramics International, Vol.33, (2007), pp.419–426.
21. S.P. Rungsarit Koonawoot, Cherdsak Saelee, Sakdiphon Thiansem, “Synthesis, control and characterization of hydroxyapatite ceramic using a solid-state reaction”, Mae Fah Luang University International Conference 2012.
22. S.H. Rhee, “Synthesis of hydroxyapatite via mechanochemical treatment”, Biomaterials, Vol.23, (2002), pp.1147–1152.

23. C. Shu, W. Yanwei, L. Hong, P. Zhengzheng, Y. Kangde, “Synthesis of carbonated hydroxyapatite nanofibers by mechanochemical methods”, Ceramic International, Vol.31, (2005), pp.135-138.
24. D. Bayraktar, A.C. Tas, A. Cu, È. Tas, Chemical preparation of carbonated calcium hydroxyapatite powders at 37C in urea-containing synthetic body fluids”, Journal of European Ceramic Society, Vol.19, (1999), pp.2573–2579.
25. A. Bigi, E. Boanini, B. Bracci, A. Facchini, S. Panzavolta, F. Segatti, L. Sturba, “Nanocrystalline hydroxyapatite coatings on titanium: a new fast biomimetic method”, Biomaterials, Vol.26, (2005), pp.4085–4089.
26. R. Drevet, H. Benhayoune, “Pulsed electrodeposition for the synthesis of strontium substituted calcium phosphate coatings with improved dissolution properties”, Materials Science Engineering community, Vol.33, (2013), pp.4260–4265.
27. M. Manso, C. Jiménez, C. Morant, P. Herrero, J. Martínez-Duart, “Electrodeposition of hydroxyapatite coatings in basic conditions”, Biomaterials, Vol.21, (2000), pp.1755–1761.
28. P. Sakthivel, A. Ragu, “Synthesis and characterization of nano hydroxyapatite with polymer matrix nano composite for biomedical applications”, International Journal of Chemical, Environmental and Biological Sciences, Vol.3, (2015), pp.383–385.
29. M. Salarian, M. Solati-Hashjin, S.S. Shafiei, R. Salarian, Z.A. Nemati, “Template-directed hydrothermal synthesis of dandelion-like hydroxyapatite in the presence of cetyltrimethylammonium bromide and polyethylene glycol”, Ceramics International, Vol.35, (2009), pp.2563–2569.

30. S. Bose, S.K. Saha, “Synthesis and characterization of hydroxyapatite nanopowders by emulsion technique’, Chemistry of Materials, Vol.15, (2003), pp.4464–4469.
31. S. Jarudilokkul, W. Tanthapanichakoon, V. Boonamnuayvittaya, “Synthesis of hydroxyapatite nanoparticles using an emulsion liquid membrane system”, Colloids and Surfaces A: Physicochemical and Engineering Aspects, Vol.296, Issues 1–3, (2007), pp.149-153.
32. G.H. An, H.J. Wang, B.H. Kim, Y.G. Jeong, Y.H. Choa, “Fabrication and characterization of a hydroxyapatite nanopowder by ultrasonic spray pyrolysis with salt assisted decomposition”, Materials Science and Engineering: A, Vol.448–451, (2007), pp.821–824.
33. M. Honda, K. Kikushima, Y. Kawanobe, T. Konishi, M. Mizumoto, M. Aizawa, “Enhanced early osteogenic differentiation by silicon-substituted hydroxyapatite ceramics fabricated via ultrasonic spray pyrolysis route’, Journal of Materials Science: Materials in Medicine, Vol.23, Issue 12, (2012), pp.2923–2932.
34. Amit Kumar Nayak, “Hydroxyapatite Synthesis Methodologies: An Overview”, International Journal of Chemistry Technology Research, Vol.2, No.2, (2010), pp 903-907.
35. Synthesis Method of Hydroxyapatite, Sophie Cox, www.ceram.com 2014.
36. Cunniffe, G.M., et al., “The synthesis and characterization of nanophase hydroxyapatite using a novel dispersant-aided precipitation method”, Journal of Biomedical Materials Research Part A, Vol.95A, No.4, (2010), pp.1142-1149.
37. Khelendra Agrawal, Gurbhinder Singh, Satya Prakash and Devendra Puri, “Synthesis of Ha by Various Sol-Gel Techniques and Their Comparison: A Review”,

International Journal of Surface Engineering & Materials Technology, Vol.2, No.1, (2012).

38. Anbalagan Balamurugan, Jean Michel, Joël Fauré, Hicham Benhayoune, Laurence Wortham Ganesh Sockalingum, Vincent Banchet, Sylvie Bouthors, Dominique Laurentmaquin, Gérard Balossier, "Synthesis and Structural Analysis of Sol Gel Derived Stoichiometric Monophasic Hydroxyapatite", Ceramics Silikáty, Vol.50, No.1, (2006), pp.27-31.
39. U. Vijayalakshmi, and S. Rajeswari, "Preparation and Characterization of Microcrystalline Hydroxyapatite Using Sol Gel Method", Trends Biomater. Artif. Organs, Vol 19, No.2, (2006), pp. 57-62.
40. Jiménez Flores, Yolanda & Camacho, Nicolette & Rojas-Trigos, José & Suárez, M, "Synthesis and Thermal Characterization of Hydroxyapatite Powders Obtained by Sol-Gel Technique", Characterization of Metals and Alloys, Chapter 14, ISBN 978-3-319-31694-9, Springer International Publishing Switzerland, (2017), pp. 167-180.
41. Hongjian Zhou, and Jaebeom Lee, "Nanoscale hydroxyapatite particles for bone tissue engineering", Acta Biomaterialia, Vol.7, (2011), pp. 2769–2781.
42. L. M. Rodrı´guez-Lorenzo, and M. Vallet-Regf, "Controlled Crystallization of Calcium Phosphate Apatites", Chem. Mater. Vol.12, (20000, pp. 2460-2465.
43. F. Mohandes, M. Salavati-Niasari, "Particle size and shape modification of hydroxyapatite nanostructures synthesized via a complexing agent-assisted route", Materials Science and Engineering. Materials for Biological applications, C.40, (2014), pp.288–298.

44. N. Reznikov, H. Chase, Y. Ben Zvi, V. Tarle, M. Singer, V. Brumfeld, R. Shahar, S. Weiner, “Inter-trabecular angle: a parameter of trabecular bone architecture in the human proximal femur that reveals underlying topological motifs”, Acta Biomaterialia, Vol.44, (2016), pp.65-72.
45. Nazeer, Muhammad Anwaar, Emel Yilgor, Mustafa Baris Yagci, Ugur Unal and Iskender Yilgor. “Effect of reaction solvent on hydroxyapatite synthesis in sol–gel process.” Royal Society open science (2017).
46. Basam A.E. Ben-Arfa, Isabel M. Miranda Salvado, José M.F. Ferreira, Robert C. Pullar, “Novel route for rapid sol-gel synthesis of hydroxyapatite, avoiding ageing and using fast drying with a 50-fold to 200-fold reduction in process time”, Materials Science and Engineering C.70 (2017), pp.796–804.
47. Lezli Matto, Lílian Paiva, Alexandre Antunes Ribeiro, Marize Varella, Magna Monteiro, “Effects of Drying Methods on The Microstructure of Biphasic Calcium Phosphate Ceramics Obtained by Sol-Gel”, 14th Congress of the Latin American Society of Biomaterials, Artificial Organs and Tissue Engineering – SLABO, 5th Edition of the Workshop on Biomaterials, Artificial Organ and Tissue Engineering, August (2017), Brazil.
48. Wojciech L. Suchanek1, and Richard E. Riman, “Hydrothermal Synthesis of Advanced Ceramic Powders”, Advances in Science and Technology Vol. 45 (2006) pp. 184-193.
49. Rustum Roy, “Accelerating the kinetics of Low-Temperature Inorganic Syntheses”, Journal of Solid State Chemistry, Vol.111, (1994), pp.11-17.

50. Yoshimura, M. and K. Byrappa, “Hydrothermal processing of materials: past, present and future”, Journal of Materials Science, Vol.43, issue.7, (2008), p.2085-2103.

51. Jun Wang, Ying & Lai, Chen & Wei, Kun & Chen, Xiaofeng & Ding, Yong & Wang, Zhong, “Investigations on the formation mechanism of hydroxyapatite synthesized by the solvothermal method”, Nanotechnology, Vol.17, issue.17, (2006), p.4405-4412.

52. Matthew Bilton, Steven J. Milne, Andrew P. Brown, “Comparison of Hydrothermal and Sol-Gel Synthesis of Nano-Particulate Hydroxyapatite by Characterization at the Bulk and Particle Level”, Open Journal of Inorganic Non-metallic Materials, Vol.2, (2012), p.1-10.

53. Saheb Ali Manafi, and Sedigheh Joughehdoust, “Synthesis of Hydroxyapatite Nanostructure by Hydrothermal Condition for Biomedical Application”, Iranian Journal of Pharmaceutical Sciences, Vol.5, No.2, (2009), pp.89-94

54. Ine´s S. Neira, Yury V. Kolen’ko, Oleg I. Lebedev, Gustaaf Van Tendeloo , Himadri S. Gupta, Francisco Guitia´n, and Masahiro Yoshimura, “ An Effective Morphology Control of Hydroxyapatite Crystals via Hydrothermal Synthesis”, Crystal Growth & Design, Vol. 9, No.1, (2009), pp. 466-467.

55. Salima Ziani, Samira Meski, and Hafit Khireddine, “Characterization of Magnesium-Doped Hydroxyapatite Prepared by Sol-Gel Process”, Int. J. Appl. Ceram. Technol., Vol.11, No.1, (2014), pp. 83–91.

56. Caibao Xue1, Yingzhi Chen, Yongzhuo Huang, and Peizhi Zhu, “Hydrothermal Synthesis and Biocompatibility Study of Highly Crystalline Carbonated Hydroxyapatite Nanorods”, Nanoscale Research Letters, Vol.10, (2015), pp.316

57. Ying Jun Wang, Jing Di Chen, Kun Wei, Shu Hua Zhang, Xi Dong Wang, "Surfactant-assisted synthesis of hydroxyapatite particles, Materials Letters, Vol. 60, (2006), pp. 3227-3231.

58. Mohammad Hossein Esnaashary, Mohammad Hossein Fathi, and Mahdi Ahmadian, "The Effect of the Two-Step Sintering Process on Consolidation of Fluoridated Hydroxyapatite and its Mechanical Properties and Bioactivity", International Journal of Applied Ceramic Technology, Vol.11, issue.1, (2014), pp.47–56.

59. A. Hanifi, M. H. Fathi, and H. Mir Mohammad Sadeghi, "Effect of Strontium Ions Substitution on Gene Delivery Related Properties of Calcium Phosphate Nanoparticles," Journal of Materials Science: Materials in Medicine, Vol.21, (2010), pp.2601–2609.

60. Y. Chen and X. Miao, "Thermal and Chemical Stability of Fluorohydroxyapatite Ceramics with Different Fluorine Contents," Biomaterials, Vol.26, (2005), pp.1205–1210.

61. S. Kannan, F. Goetz-Neunhoeffer, J. Neubauer, and J. M. F. Ferreiraw, "Ionic substitutions in Biphasic Hydroxyapatite and β- Tricalcium Phosphate mixtures: Structural analysis by Rietveld Refinement", J. Am. Ceram. Soc., Vol.91, No.1, (2008), pp. 1–12.

62. S. Ramesh, C.Y. Tan, C.L. Peralta, and W.D. Teng, "The effect of manganese oxide on the sinterability of hydroxyapatite", Science and Technology of Advanced Materials, Vol.8, (2007), pp. 257–263.

63. Czesława Paluszkiewicz, Anna S´ losarczyk, Dawid Pijocha, Maciej Sitarz, Mirosław Buc´ko Aneta Zima, Anna Chros´cicka, and Małgorzata Lewandowska-Szumieł,

"Synthesis, structural properties and thermal stability of Mn-doped hydroxyapatite", Journal of Molecular Structure, Vol.976, (2010), pp.301–309

64. Isaac Mayer, Orit Jacobsohn, Tamara Niazov, Jacques Werckmann, Monica Iliescu, Mireille Richard-Plouet, Olaf Burghaus, and Dirk Reinen, "Manganese in Precipitated Hydroxyapatites", Eur. J. Inorg. Chem., (2003), pp. 1445-1451.
65. Hanan H. Beheri, Khaled R. Mohamed, Gehan T. El-Bassyouni, "Mechanical and microstructure of reinforced hydroxyapatite/calcium silicate nano-composites materials", Materials and Design, Vol. 44, (2013), pp. 461–468.
66. A.J. Ruys, "Silicon-Doped Hydroxyapatite", Journal of Australian Ceramic society, Vol.29, no.1/2, (1995), pp.71- 80.
67. Abdulsalam Khashan Swadi , Zuhair Wahib Jassim, Mohamed Ubaid Kadum, Mutawar Redha Mohamed Ali, "Influence of Fluoride Addition on Hydroxyapatite Prepared for Medical Applications", Baghdad Science Journal, Vol. 9, No.3, (2012), pp.541-546.
68. Anna Strunecká, Jiří Patočka, Paul Connett, "Fluorine in Medicine", Journal of Applied Biomedicine, Vol. 2, (2004), pp.141-150.
69. D.S Morais, S.Fernandes, P.S. Gomes, M.H Fernandes, P. Sampaio, M. P Ferraz, J.D Santos, M. A Lopes, and N. Sooraj Hussain, "Novel cerium doped glass-reinforced hydroxyapatite with antibacterial and osteoconductive properties for bone tissue regeneration", Biomed. Mater. Vol. 10, (2015).
70. Amit Bandyopadhyay, Susmita Bose, and Suman Das, "3D printing of biomaterials", MRS Bulletin, Vol, 40, (2015), pp. 108-115

71. Vincenzo Guarino, Filippo Causa, Luigi Ambrosio, “Bioactive scaffolds for bone and ligament tissue”, Expert Review of Medical Devices, Vol.4, issue.3, (2007), pp.405–418.

72. Lutz-Christian Gerhardt, and Aldo R. Boccaccini, “Bioactive Glass and Glass-Ceramic Scaffolds for Bone Tissue Engineering”, Materials, Vol.3, (2010), pp.3867–3910.

73. H. Seitz, W. Rieder, S. Irsen, B. Leukers and C. Tille, “Three-dimensional printing of porous ceramic scaffolds for bone tissue engineering”, Journal of Biomedical Materials Research, Part B- Applied Biomaterials, Vol.74, (2005), pp.782–788.

74. S. Lei, M. C. Frank, D. D. Anderson and T. D. Brown, “A Method to Represent Heterogeneous Materials for Rapid Prototyping: The Matryoshka Approach”, Rapid Prototyping Journal, Vol.20, (2014), pp.390–402.

75. Xiaoyu Du,a Shengyang Fua and Yufang Zhu, “3D printing of ceramic-based scaffolds for bone tissue engineering: an overview”, Journal of Materials Chemistry B, Vol.6, (2018),pp.4397.

76. N N Razali, M.A Sukardi, I Sopyan, M. Mel, H M Salleh, and M M. Rahman, “The effects of excess calcium on the handling and mechanical properties of hydrothermal derived calcium phosphate bone cement”, Materials Science and Engineering, Vol.290, issue.1, (2017), pp.12053.

77. Bohner M, “Reactivity of calcium phosphate cements”, Journal of Materials Chemistry, Vol.17, (2007), pp.3980-3986.

78. Gbureck U, Barralet JE, Hofmann M and Thull, “Mechanical Activation of Tetracalcium Phosphate”, Journal of American Ceramic Society, Vol.87, issue.2, (2004), pp.311–313.

79. Xin Wang, Man Jiang, Zuowan Zhou, Jihua Gou, David Hui, “3D printing of polymer matrix composites: A review and prospective”, Composites Part B, Vol.110, (2017), pp.442-458.

80. Murphy SV, Atala A, “3D Bioprinting Of Tissues and Organs”, Nature Biotechnology, Vol.32, issue.8, (2014), pp.773-785.

81. Kumar S, Kruth J-P, “Composites by Rapid Prototyping Technology”, Materials and Design, Vol.31, issue.2, (2010), pp.850-856.

82. Gonçalves EM, Oliveira FJ, Silva RF, Neto MA, Fernandes MH, Amaral M, Vallet-Regí M, Vila M, “Three-dimensional printed PCL-hydroxyapatite scaffolds filled with CNTs for bone cell growth stimulation”, Journal of Biomedical Materials Research. Part B Applied Biomaterials, Vol.104, issue.6, (2016), pp.121-129.

83. Kim J, McBride S, Tellis B, Alvarez-Urena P, Song Y-H, Dean DD, Sylvia VL, Elgendy H, Ong J, Hollinger JO, “Rapid-prototyped PLGA/b-TCP/hydroxyapatite nanocomposite scaffolds in a rabbit femoral defect model”, Biofabrication, Vol.4, issue.2, (2012), pp.25003.

84. Xia Y, Zhou P, Cheng X, Xie Y, Liang C, Li C, Xu S, “Selective laser sintering fabrication of nano-hydroxyapatite/poly-ε-caprolactone scaffolds for bone tissue engineering applications”, International Journal of Nanomedicine, Vol.8, (2013), pp.4197.

85. Qinghua Wei, YanenWangn, XinpeiLi, MingmingYang, Weihong Chai, Kai Wang, Yingfeng zhang, “Study the bonding mechanism of binders on hydroxyapatite surface and mechanical properties for 3DP fabrication bone scaffolds”, Journal of the Mechanical Behavior of Biomedical Materials, Vol.57, (2016), pp.190-200.

86. Guobao Weia, and Peter X. Maa, “Structure and properties of nano-hydroxyapatite/polymer composite scaffolds for bone tissue engineering”, Biomaterials, Vol. 25, (2004), pp. 4749-4757.

87. J. Suwanprateeb, R. Sanngam, W. Suwanpreuk, “Fabrication of bioactive hydroxyapatite/bis-GMA based composite via three-dimensional printing”, J Mater Sci: Mater Med, Vol. 19, (2008), pp.2637-2645.

88. F. Sarsilmaz, N. Orhan, E. Unsaldi, A.S. Durmus, N. Colakoglu, “A polyethylene-high proportion hydroxyapatite implant and its investigation in vivo” Acta of Bioengineering and Biomechanics, Vol. 9, No. 2, (2007), pp.9-16.

89. R. Chumnanklang, T. Panyathanmaporn, K. Sitthiseripratip, J. Suwanprateeb, “3D printing of hydroxyapatite: Effect of binder concentration in pre-coated particle on part strength”, Materials Science and Engineering, Vol. 27, (2007), pp. 914-921.

90. Lin Sun, Sara T. Parker, Daisuke Syoji, Xiuli Wang, Jennifer A. Lewis, and David L. Kaplan, “Direct-Write Assembly of 3D Silk/Hydroxyapatite Scaffolds for Bone Co-Cultures”, Adv. Healthcare Mater, Vol. 1, (2012), pp. 729-735.

91. Gregory M.Gratson, Mingjie Xu, Jennifer A. Lewis, “Microperiodic structures: Direct writing of three-dimensional webs”, Nature 428, 386, (2004).

92. Sarah Michnaa, Willie Wua, and Jennifer A. Lewis, “Concentrated hydroxyapatite inks for direct-write assembly of 3-D periodic scaffolds”, Biomaterials, Vol. 26, (2005), pp. 5632-5639.

93. Yongxiang Luo, Anja Lode, Chengtie Wu, Jiang Chang, and Michael Gelinsky, “Alginate-Nano hydroxyapatite Scaffolds with Designed Core-Shell structures fabricated by 3D plotting and in situ mineralization for bone tissue engineering”, ACS Appl. Mater. Interfaces, Vol. 7, (2015), pp. 6541-6549.

94. Alok Kumar, Ashwini R Akkineni, Bikramjit Basu, and Michael Gelinsky “Three-dimensional plotted hydroxyapatite scaffolds with predefined architecture: comparison of stabilization by alginate cross-linking versus sintering”, Journal of Biomaterials Applications, Vol. 30, No.8, (2016), pp.1168-1181.

95. Uwe klammert, Uwe Gbureck, Elke Vorndran, Jan Rodiger, Philipp Meyer-Marcotty, Alexander C. Kubler, “3D powder printed calcium phosphate implants for reconstruction of cranial and maxillofacial defects”, Journal of Cranio-Maxillo-Facial Surgery, Vol. 38, (2010), pp. 565-570.

96. Vassilis Karageorgiou, and David Kaplan, “Porosity of 3D biomaterial scaffolds and osteogenesis”, Biomaterials, Vol. 26, (2005), pp.5474-5491

97. Best, S., Sim, B., Kayser, M., Downes, S, “Dependence of osteoblastic response on variations in the chemical composition and physical properties of hydroxyapatite”, Journal of Materials Science. Materials in Medicine, Vol.8, issue.2, (1997), pp.97–103.

98. Eggli, P.S., Muller, W., Schenk, R.K, “Porous hydroxyapatite and tricalcium phosphate cylinders with two different pore size ranges implanted in the cancellous

bone of rabbits", Clinical Orthopaedic Related Research, Vol.232, (1988), pp.127–138.

99. Rupita Ghosh & Ritwik Sarkar, "Synthesis and characterization of sintered hydroxyapatite: a comparative study on the effect of preparation route", Journal of the Australian Ceramic Society, Vol.54, issue.1, (2018), pp. 71-80.

100. Harabi, A., Harabi, E, "A modified milling system, using a bimodal distribution of highly resistant ceramics-part 1. A natural hydroxyapatite study", Materials Science and Engineering. C, Materials for Biological Applications, Vol.7, (2015), pp.206-215.

101. Mythili Prakasam, Janis Locs, Kristine Salma-Ancane, Dagnija Loca, Alain Largeteau, and Liga Berzina-Cimdina, "Properties and Applications of Dense Hydroxyapatite: A Review", Journal of Functional Biomaterials, Vol.6, issue.4, (2015), pp.1099-1140.

102. E. Champion, "Sintering of Calcium Phosphate Bioceramics", Acta Biomaterialia, Vol.9, issue.4, (2013), pp.5855–5875

103. Kobayashi, S.; Kawai, W.; Wakayama, S, "The effect of pressure during sintering on the strength and the fracture toughness of hydroxyapatite ceramics", Journal of Materials Science. Materials in Medicine, Vol.17, (2006), pp.1089–1093.

104. Li, J.G, Hashida, T, "In situ formation of hydroxyapatite-whisker ceramics by hydrothermal hot-pressing method", Journal of American Ceramic Society, Vol.89, (2006), pp.3544–3546.

105. Ramesh, S, Tan C.Y., Sopyan, I, Hamdi, M, Teng, W.D, “Consolidation of nanocrystalline hydroxyapatite powder”, Science and Technology of Advance Materials, Vol.8, issue.1, (2007), pp.124–130.

106. Raynaud S, Champion E, Bernache Assollant D, Thomas P, “Calcium phosphate apatites with variable Ca/P atomic ratio I. Synthesis, characterization and thermal stability of powders”, Biomaterials, Vol.23, (2002), pp.1065–1072.

107. Liao CJ, Lin FH, Chen KS, Sun JS, “Thermal decomposition and reconstruction of hydroxyapatite in air atmosphere”, Biomaterials, Vol.20, (1999), pp.1807–1813.

108. Wang PE, Chaki TK, “Sintering behavior and mechanical properties of hydroxyapatite and dicalcium phosphate”, Journal of Materials Science. Materials in Medicine, Vol.4, (1993), pp.150–158.

109. M. N. Rahaman,” Ceramic Processing and Sintering”, Marcel Dekker Inc, New York, 2005, ISBN-13: 978-0824709884

110. Chen IW, Wang XH, “Sintering Dense Nanocrystalline Ceramics Without Final Stage Grain Growth”, Nature, Vol.404, (2000), pp.168–170.

111. X. Wang, P. Chen, and I. Chen, “Two-Step Sintering of Ceramics with Constant Grain-Size, I. Y2O3,” Journal of American Ceramic Society, Vol.89, (2006), pp.431–437.

112. Feray Bakan, Oral Laçin, and Hanifi Sarac, “A novel low temperature sol–gel synthesis process for thermally stable nano crystalline hydroxyapatite”, Powder Technology, Vol. 233, (2013), pp.295-302.

113. Yingjun Wang, Shuhua Zhang, Kun Wei, Naru Zhao, Jingdi Chen, and Xudong Wang, “Hydrothermal synthesis of Hydroxyapatite nanopowder using cationic surfactant as a template”, Materials Letters, Vol. 60, (2006), pp.1484-1487.

114. ASTM E384-16 Standard Test Method for Microindentation Hardness of Materials, ASTM International, West Conshohocken, PA, 2016.

115. Matthew Bilton, Steven J. Milne, Andrew P. Brown, “Comparison of Hydrothermal and Sol-Gel Synthesis of Nano-Particulate Hydroxyapatite by Characterisation at the Bulk and Particle Level”, Open Journal of Inorganic Non-metallic Materials, Vol.2, (2012), pp.1-10.

116. Gérrard Eddy Jai Poinern, Ravi Krishna Brundavanam, Xuan Thi Le, Derek Fawcett, “The Mechanical Properties of a Porous Ceramic Derived from a 30 nm Sized Particle Based Powder of Hydroxyapatite for Potential Hard Tissue Engineering Applications”, American Journal of Biomedical Engineering, Vol.2, issue.6, (2012), pp.278-286.

117. V.M. Rusu, C.H. Ng, M. Wilke, B. Tiersch, P. Fratzl, M.G. Peter, “Size Controlled Hydroxyapatite Nanoparticles as Self-Organised Organic-Inorganic Composite Materials”, Biomaterials, Vol.26, (2005), pp.5414-5426.

118. Karin A. Hing, “Bone repair in the twenty-first century: biology, chemistry or engineering?”, Philosophical Transactions of Royal Society of London. Series A, Mathematical, Physical, Engineering, and Science, Vol.362, issue.1825, (2004), pp.2821-2850.

119. Masoume Nazarpak, Mehran Solati-Hashjin, and Fatollah Moztarzadeh, “Characterization of Hydroxyapatite Blocks for Biomedical Applicatons”,

Biomedical Engineering,Trends, Research, and technologies, (2011), ISBN: 978-953-307-514-3.

120. J Liu, X Ye, H Wang, M Zhu, B Wang, H Yan, "The Influence of pH and Temperature on the Morphology of Hydroxyapatite Synthesised by Hydrothermal Method", Ceramics International, Vol. 29, (2003), pp. 629 – 633.

121. R. Kumar, K. H. Prakash, P. Cheang, and K. A. Khor, "Temperature Driven Morphological Changes of Chemically Precipitated Hydroxyapatite Nanoparticles", Langmuir, Vol. 20, (2004), pp. 5196 – 5200.